

**Development of Numerical Codes for Modeling Electromagnetic  
Behavior At High Frequencies Near Large Objects**

Principal Investigator: R. P. Joshi  
Department of Electrical and Computer Engineering  
Old Dominion University, Norfolk, VA 23529-0246

NASA Technical Monitor: Dr. M. D. Deshpande  
Electromagnetics Research Branch, Airborne Systems Competency  
NASA Langley, Hampton, VA 23681

**FINAL REPORT**  
**January, 2003.**

# CONTENTS

Topic	Page
Abstract	3
I. Introduction and Problem Statement	4
II. Theoretical Background of the Moment Method	7
II.A Simple Planar Surfaces for the Moment Method	8
II.B Evaluation of the Matrix Elements	11
II.C Example of Incident Plane Wave for the Moment Method	14
III. Aspects of Physical Optics and the Hybrid MM-PO Scheme	14
III.A Matrix Elements for the Hybrid MM-PO Scheme	17
IV. The Finite-Difference, Time-Domain (FDTD) Method	20
V. Validation of the FDTD Numerical Implementation	25
VI. The Alternating Direction Implicit (ADI) FDTD Method	27
VII. Simple Example Implementations and Results	32
VII.A The MM Scheme and Calculations	32
VIII. Results for the FDTD Scheme	37
IX. Results for the Three-Dimensional ADI-FDTD Scheme	42
X. Summary and Potential Future Work	48
XI. References	50

## **Abstract**

A study into the problem of determining electromagnetic solutions at high frequencies for problems involving complex geometries, large sizes and multiple sources (e.g. antennas) has been initiated. Typical applications include the behavior of antennas (and radiators) installed on complex conducting structures (e.g. ships, aircrafts, etc..) with strong interactions between antennas, the radiation patterns, and electromagnetic signals is of great interest for electromagnetic compatibility control. This includes the overall performance evaluation and control of all on-board radiating systems, electromagnetic interference, and personnel radiation hazards.

Electromagnetic computational capability exists at NASA LaRC, and many of the codes developed are based on the Moment Method (MM). However, the MM is computationally intensive, and this places a limit on the size of objects and structures that can be modeled. Here, two approaches are proposed: (i) a current-based hybrid scheme that combines the MM with Physical optics, and (ii) an Alternating Direction Implicit-Finite Difference Time Domain (ADI-FDTD) method. The essence of a hybrid technique is to split the overall scattering surface(s) into two regions: (a) a MM zone (MMZ) which can be used over any part of the given geometry, but is most essential over irregular and “non-smooth” geometries, and (b) a PO sub-region (POSR). Currents induced on the scattering and reflecting surfaces can then be computed in two ways depending on whether the region belonged to the MMZ or was part of the POSR. For the MMZ, the current calculations proceed in terms of basis functions with undetermined coefficients (as in the usual MM method), and the answer obtained by solving a system of linear equations. Over the POSR, conduction is obtained as a superposition of two contributions: (i) currents due to the incident magnetic field, and (ii) currents produced by the mutual induction from conduction within the MMZ. This effectively leads to a reduction in the size of linear equations from  $N$  to  $N - N_{PO}$  with  $N$  being the total number of segments for the entire surface and  $N_{PO}$  the number of segments over the POSR. The scheme would be appropriate for relatively large, flat surfaces, and at high frequencies.

The ADI-FDTD scheme provides for both transient and steady state analyses. The restrictive Courant-Friedrich-Levy (CFL) condition on the time-step is removed, and so large time steps can be chosen even though the spatial grids are small. This report includes the problem definition, a detailed discussion of both the numerical techniques, and numerical implementations for simple surface geometries. Numerical solutions have been derived for a few simple situations.

## **I. Introduction and Problem Statement :**

Research interest at NASA in the general area of electromagnetics arises from a broad range of potential applications involving detection and remote sensing, system stability with regard to electromagnetic disturbances/pulses, stochastic variability, and scattering effects in radar systems. Many of these applications rely on the use of antennas that may be mounted on or placed in close proximity to suitable platforms (for example, airplanes). It therefore, becomes important to be able to accurately analyze and predict antenna performance characteristics in the presence of such platforms and large objects involving complex geometries.

Electromagnetic solutions (including parameters such as impedance and radiation patterns) can be obtained by either the moment method [1,2], or finite-element analysis [3]. Of these, the moment method (MM) is more accurate, but computationally intensive as it leads to a dense matrix that has to be solved. The finite element method (FEM) is more attractive since it results in sparse, banded matrices which can be stored and solved more easily. However, the FEM for unbounded problems does not include the Sommerfeld radiation condition, and requires the use of adequate absorbing boundary conditions to treat the radiation conditions that must be imposed at the boundaries of the discretized region. The MM scheme is accurate but slow and computationally very intensive, especially as the physical dimensions approach lengths on the order of ten wavelengths. Moreover, MM is applicable to complex conducting or penetrable bodies, and complicated geometries. The MM requires the solution of “N” equations, where “N” the number of basis functions chosen depends on the number of patch-elements (or segments) into which the overall physical system and structure is decomposed. These “N” equations have to be solved, which typically requires storage on the order of  $N^2$  and computation times on the order of  $N^k$ , with  $2 < k < 3$  [4]. In employing basis functions, the segment length has to be taken to be smaller than  $\lambda/10$ , with  $\lambda$  being the operating wavelength. Obviously, for high-frequency situations,  $\lambda$  reduces dramatically, leading to increases in both the storage and computational requirements which scale as  $f^4$  and  $f^{2k}$ . Consequently, from a practical standpoint, the use for the MM technique is restricted to applications involving low frequencies and/or medium sized scattering bodies. At high frequencies, or for large sized bodies, the MM becomes computationally intractable.

The problem of determining electromagnetic solutions at high frequencies can be simplified by incorporating ideas of “optics”. An important premise for the optics-based techniques is that at sufficiently high frequencies the propagation, scattering and diffraction of electromagnetic signals

exhibit highly localized behavior. Such a localized behavior can qualitatively be demonstrated by considering the radiation integral over the spatial current distribution induced on a radiating object by the primary excitation. At high frequency, the integrand oscillates rapidly to produce destructive interference. The dominant contribution arises only from waves that emanate from the local neighborhood of critical areas that are points of reflection, transmission and diffraction [5]. The connection between ray optics and Maxwell's equations has also been demonstrated by deriving the laws of geometric optics from Helmholtz's scalar wave equation [6,7]. In such a simple ray treatment based solely on incident, reflected and transmitted beams, no rays can exist in the "shadow boundaries" beyond the "line-of-sight" visibility regions.

An ideal option would be the use of hybrid schemes that preserve the accuracy without computational complexity, as suggested by Thiele et al. [8], Burnside and co-workers [9], and reviewed more recently [10,11]. In general, the hybrid scheme can be formulated as a field-based (FB) or current-based (CB) analysis. In the field-based version [12,13], solutions for the fields associated with edge or surface diffraction, based on the geometrical theory of diffraction (GTD) or geometrical optics (GO), could be used as the starting point. These could serve as an Ansatz to the MM formulation and be a representation for parts of a scatterer not conforming to a canonic geometry. The FB approach is attractive for problems where the radiator is in proximity to large convex surfaces for which the canonical GTD solutions are known. These approaches are also known as "ray-based" schemes provide very fast results, but their application is restricted to problems where asymptotic high-frequency solutions are available. In these GTD-MM schemes, the form of the currents induced by straight-edge diffraction or in the shadow regions were derived from GTD. In CB formulations, the analysis proceeds from Ansatz solutions for the currents obtained from optics-theory [14], such as physical optics (PO) or the Fock theory. A Galerkin representation of the unknown currents is used in regions of the scatterer where Ansatz solutions do not exist, such as surfaces with materials and/or geometric irregularities. The CB approach can be more advantageous since the MoM is based on currents as well. Hence, a continuous current flow can be modeled on the whole surface of the scattering body. Also, since CB-based methods are inherently capable of modeling arbitrary-shaped geometries. A number of CB hybrid methods have been discussed in the literature [4, 15-17].

Here, a hybrid technique that combines the MM with aspects of PO has been used. It requires less computational work than a pure MM scheme. Such an approach would be suitable for high-

frequency analysis or for situations in which the physical dimensions of scattering objects was large. The essence of a hybrid technique would be to invoke a splitting of the overall scattering surface(s) into two regions: (i) a MM zone (MMZ) which can be used over any part of the given geometry, but is most essential over irregular and “non-smooth” geometries, and (ii) a PO sub-region (POSR). Currents induced on the scattering and reflecting surfaces could then be computed in two ways depending on whether the region belonged to the MMZ or was part of the POSR. For the MMZ, the current calculations would proceed in terms of the basis functions with coefficients determined through the solution of a linear system of equations (usual MM method). Over the POSR, a superposition of basis functions with known coefficients could be used. This could effectively lead to a reduction in the size of linear equations from  $N$  to  $N - N_{PO}$  with  $N$  being the total number of segments for the entire surface and  $N_{PO}$  the number of segments over the POSR. However, the approximations inherent in such a hybrid approach are listed below. For self-consistency and accuracy, both the self- and mutual-coupling between the MM and PO regions have to be considered.

*Assumptions Inherent in the Hybrid MM-PO Approach:*

- (i) PO approach in the illuminated region, and for a perfect electric or magnetic conductor.
- (ii) Secondary radiation due to many-body inter-coupling, creeping wave effects and edge diffraction neglected. Such effects could only be accounted for by combining the MM with other techniques such as GTD, Fock theory etc..
- (iii) PO applied only over regions of “smooth” geometry. All other irregular or “non-smooth” geometric regions assigned to the MM domain.
- (iv) Hybrid approach only valid for high frequencies or when dimensions of physical object much larger than operating wavelength.
- (v) Applicable only for linear systems i.e. media for which the permeability ( $\mu$ ), permittivity ( $\epsilon$ ) and conductivity ( $\sigma$ ) are constant and not functions of the field excitation.
- (vi) Accuracy limited by the finiteness of the basis functions – since an exact MM solution is only available in theory for an infinite basis set.

*Advantages of the ADI-FDTD Simulation Approach:*

- (i) The ADI-FDTD simulation scheme allows for both a complete time-domain analysis and the steady-state result. The latter can result by running the simulations up to longer times.

The transient behavior cannot be obtained from the Moment Method or PO-MoM schemes.

- (ii) The ADI-FDTD allows for any arbitrary geometry including sharp corners and complex features.
- (iii) It is significantly faster than the traditional FDTD scheme since very large time steps can be used without the need to be restricted to the CFL condition.
- (iv) High frequency analyses for which the spatial discretization has to be small, can be carried out relatively easily as the time-step can remain large. Similarly, the technique is of advantage for large objects for which many grid points may be required.
- (v) Non-uniform, multi-grids can be employed for better resolution.
- (vi) Absorbing boundary conditions can be implemented for accurate analyses.
- (vii) Finally, dielectrics or perfect conductors or both can be studied with ADI-FDTD. Thus, it becomes easy to look at problem that involve coatings, and multiple layers.

## II. Theoretical Background of the Moment Method :

A time-harmonic electric field  $\mathbf{E}^{\text{inc}}(\mathbf{r})$  incident on a conducting structure induces currents  $\mathbf{J}(\mathbf{r}')$  on the surface, which in turn, radiate a secondary (or scattered) field  $\mathbf{E}^{\text{sca}}(\mathbf{r})$  given by:

$$\mathbf{E}^{\text{sca}}(\mathbf{r}) = -j\omega \mathbf{A}(\mathbf{J}, \mathbf{r}) - \nabla\Phi(\rho, \mathbf{r}) , \quad (1)$$

where  $\mathbf{A}(\mathbf{J}, \mathbf{r})$  the magnetic vector potential is:

$$\mathbf{A}(\mathbf{J}, \mathbf{r}) = [\mu/(4\pi)] \int [\{\mathbf{J}(\mathbf{r}') \exp[-jkR]\}/R] dV' , \quad (2a)$$

and  $\Phi(\rho, \mathbf{r})$  the electric scalar potential is expressed as:

$$\Phi(\rho, \mathbf{r}) = [1/(4\pi\epsilon)] \int [\rho(\mathbf{r}') \exp[-jkR]\}/R] dV' , \quad (2b)$$

with  $R$  being the distance from the source point  $(\mathbf{r}')$  to the observation point  $(\mathbf{r})$ , i.e.  $R = |\mathbf{r} - \mathbf{r}'|$ . Since the tangential component of the total electric field must equal zero at the boundary of a perfect conductor, one gets:  $\mathbf{E}^{\text{tot}}(\mathbf{r})|_{\text{tan}} = \mathbf{E}^{\text{sca}}(\mathbf{r})|_{\text{tan}} + \mathbf{E}^{\text{inc}}(\mathbf{r})|_{\text{tan}} = 0 \Rightarrow \mathbf{E}^{\text{inc}}(\mathbf{r})|_{\text{tan}} = -\mathbf{E}^{\text{sca}}(\mathbf{r})|_{\text{tan}}$ . Using eqns. (1) and (2a,2b), this yields the following electric field integral equation (EFIE) for the unknown

current density  $\mathbf{J}(\mathbf{r}')$  :

$$\mathbf{E}^{\text{inc}}(\mathbf{r})|_{\text{tan}} = [j\omega\mu/(4\pi) \int [\{\mathbf{J}(\mathbf{r}')\exp[-jkR]\}/R]dV' - 1/(4\pi j\omega\epsilon) \nabla \{ \int \nabla \cdot \mathbf{J}(\mathbf{r}') \exp[-jkR]/R \} dV']|_{\text{tan}} , \quad (3)$$

Where the continuity equation:  $\rho(\mathbf{r}') = -1/(j\omega) \nabla \cdot \mathbf{J}(\mathbf{r}')$  has been used to relate the charge density  $\rho(\mathbf{r}')$  to the current density  $\mathbf{J}(\mathbf{r}')$ .

In this EFIE formulation, the current density  $\mathbf{J}(\mathbf{r}')$  is the unknown to be solved, given a complete specification of the incident electric field  $\mathbf{E}^{\text{inc}}(\mathbf{r})$ . The EFIE, which a linear integro-differential equation has the following general form:  $Lf(x) = g(x)$ , where  $g(x)$  denotes the incident E-field excitation and  $f(x)$  the unknown currents. The moment method (MM) consists of converting the EFIE into a matrix equation that can be solved for the unknown currents [1]. This is done by expanding the unknown  $f(x)$  in terms of a finite number of sub-domain basis function  $f_{Bi}(x)$  as:  $f(x) = \sum_{i=1}^N a_i f_{Bi}(x)$ . Using these basis functions in the EFIE, and taking an inner product with of both sides with respect to testing functions  $f_{Tj}(x)$  converts the integral equation into a system of  $N$  equations in the  $N$ -unknowns  $a_i$ . Thus, for example,

$$\sum_{i=1}^N a_i \langle f_{Tj}(x), Lf_{Bi}(x) \rangle = \langle f_{Tj}(x), g(x) \rangle , \quad j = 1, 2, \dots, N \quad , \quad (4)$$

i.e.  $[L_{ji}] [a_i] = [g_j]$  .

By determining the unknown coefficients  $a_i$ , the desired solution  $f(x)$  to the EFIE is obtained. Usually, the test functions are taken to be the same as the basis functions [i.e.  $f_{Tj}(x) = f_{Bj}(x)$ ] to ensure that the matrix  $[L]$  is nonsingular.

## II.A Simple Planar Surfaces for the Moment Method :

In general, the electromagnetic scattering problems of interest present the following four types of structures [18] : (i) Surfaces – planar or curved, (ii) wires as in current driven wire antennas, (iii) wire-wire junctions, and (iv) surface-wire junctions. The basis functions  $\mathbf{B}_n(\mathbf{r})$  for surfaces were first proposed by Rao et al. [19] and describe current flow on a surface between triangular patches. One basis function is associated with the  $n^{\text{th}}$  edge and is defined to be:



$$\begin{aligned} \mathbf{B}_n(\mathbf{r}) &= \{L_n / (2A_{n\pm})\} \rho_{n\pm} , \quad \text{for } \mathbf{r} \in T_{n\pm} \\ &= 0 , \quad \text{elsewhere} , \end{aligned} \quad (5)$$

where  $L_n$  is the common edge between two triangles  $T_{n+}$  and  $T_{n-}$ , having areas  $A_{n\pm}$ , respectively. The global position  $\mathbf{r}$  and the local position vectors  $\rho_{n\pm}$  are shown in Fig. 1. The reference direction of current flow is from  $T_{n+}$  to  $T_{n-}$  and the total charge associated with each pair of triangles is zero [18].

Basis functions for wires, wire-surface junctions and wire-wire junctions have similarly been determined in the literature, and can be found in a review report by Veihl and Mittra [18]. However, the details are not given here in this interim report. The omission arises from a desire to keep the structures simple during this initial developmental stage, and because the MM-PO formulation has only been applied thus far to surfaces. Based on the reports in the literature (e.g. [18]), In the near the calculations can easily be extended to include other physical structures (such as wires and wire-surface junctions) in the near future.

Using the surface basis functions, as a concrete yet simple demonstrative example, the current  $\mathbf{J}(\mathbf{R})$  can be expressed in terms of the bases  $\mathbf{B}_i(\mathbf{r})$  as:  $\mathbf{J}(\mathbf{R}) = \sum_1^N \mathbf{I}_i(\mathbf{r}) \mathbf{B}_i(\mathbf{r})$ . It must be mentioned, that here again for simplicity, only a single surface has been considered. For multiple surfaces, the above single sum will transform over to a double summation. Consequently, the scattered electric field  $\mathbf{E}^{sc}(\mathbf{r})$  can be expressed in terms of the vector and scalar potentials and the bases functions as:

$$\mathbf{E}^{sc}(\mathbf{r}) = \sum_1^N \mathbf{I}_i \mathbf{E}_i(\mathbf{r}) , \quad (6a)$$

$$\text{where, } \mathbf{E}_i(\mathbf{r}) = -j \omega \mathbf{A}_i(\mathbf{r}) - \nabla \Phi_i(\mathbf{r}) , \quad (6b)$$

$$\mathbf{A}_i(\mathbf{r}) = \mu \iint_{S'} \mathbf{B}_i(\mathbf{r}') G(\mathbf{r}, \mathbf{r}') dS' , \quad (6c)$$

$$\text{and, } \Phi_i(\mathbf{r}) = (1/\epsilon) \iint_{S'} b_i(\mathbf{r}') G(\mathbf{r}, \mathbf{r}') dS' , \quad (6d)$$

where as given in [18],  $b_i(\mathbf{r}') = -[1/(j \omega)] \nabla \cdot \mathbf{B}_i(\mathbf{r}')$ . For the surface basis functions of eqn. (5),  $b_i(\mathbf{r}') = -\{ \pm L_n / (j \omega A_{n\pm}) \}$  for  $\mathbf{r}' \in T_{n\pm}$ , and  $b_i(\mathbf{r}') = 0$  elsewhere. In eqns. (6c) and (6d) above,  $G(\mathbf{r}, \mathbf{r}')$  is the free space Green's function given by:

$$G(\mathbf{r}, \mathbf{r}') = \exp[-jkR] / (4\pi R) , \quad (6e)$$

with  $R = |\mathbf{r} - \mathbf{r}'|$ . Substitution of the Green's function and the surface basis function  $\mathbf{B}_i(\mathbf{r}')$  from eqn. (5) into eqns. (6) leads to the following expressions for the vector and scalar potentials:

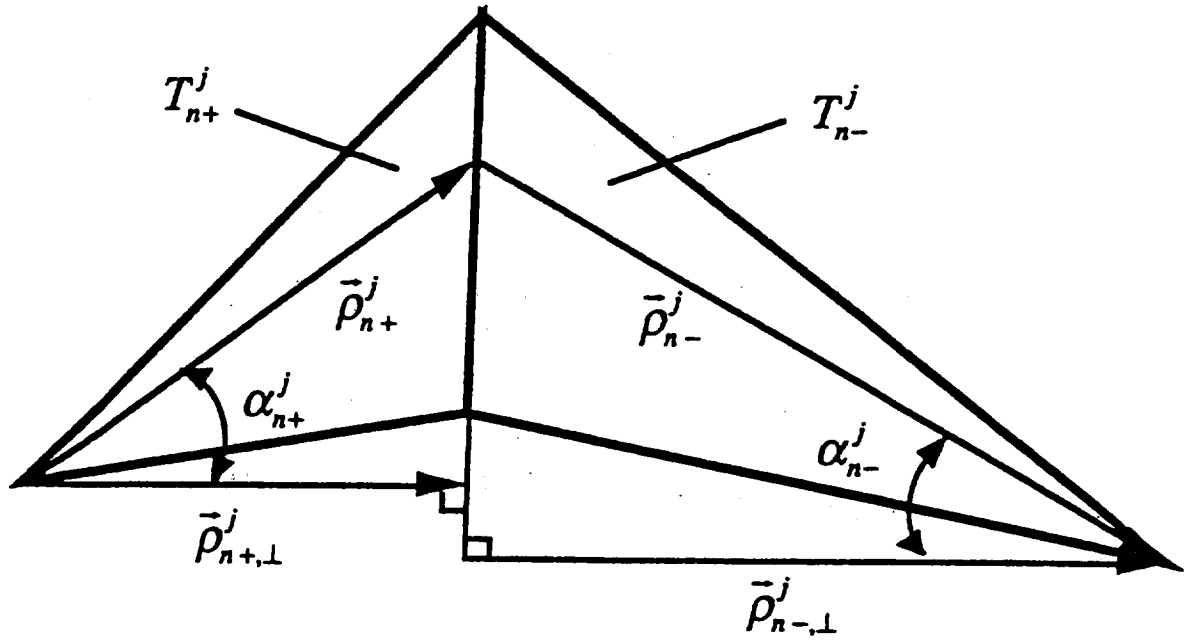


Fig. 1. Definition of the surface basis functions  $\mathbf{B}_n(\mathbf{r})$  in terms of the global co-ordinates associated with the origin O. The triangles  $T_{n+}$  and  $T_{n-}$  on either side of the common boundary (i.e. the  $n^{\text{th}}$  edge) having length  $L_n$  are shown [after reference 18].

$$\mathbf{A}_i(\mathbf{r}) = \{1/(4\pi)\} [\iint_{S'+} [L_i/(2A_i+R)] \exp[-jkR] \rho_{i+} dS' + \iint_{S'-} [L_i/(2A_i-R)] \exp[-jkR] \rho_{i-} dS'] , \quad (7a)$$

$$\text{and, } \Phi_i(\mathbf{r}) = \{-1/(4\pi j\omega\epsilon)\} [\iint_{S'+} [L_i/(A_i+R)] \exp[-jkR] dS' - \iint_{S'-} [L_i/(A_i-R)] \exp[-jkR] dS'] . \quad (7b)$$

Since  $\mathbf{E}^{\text{inc}} = -\mathbf{E}^{\text{sca}}$ , the governing MM equation becomes:  $\langle \mathbf{E}^{\text{inc}} \cdot \mathbf{B}_n \rangle = \sum_{i=1}^N \mathbf{I}_i \langle \mathbf{B}_n \cdot (j\omega \mathbf{A}_i + \nabla \Phi_i) \rangle$ . The use of (5) for the bases vectors and the one-point approximation for the surface integral at the centroid, leads to:

$$\langle \mathbf{E}^{\text{inc}} \cdot \mathbf{B}_n \rangle = (L_n/2) [ \mathbf{E}^{\text{inc}}(\mathbf{r}_{\text{cn}+}) \cdot \rho_{\text{cn}+} + \mathbf{E}^{\text{inc}}(\mathbf{r}_{\text{cn}-}) \cdot \rho_{\text{cn}-} ] , \quad (8a)$$

$$\langle \mathbf{B}_n \cdot (j\omega \mathbf{A}_i) \rangle = (j\omega L_n/2) [ \mathbf{A}_i(\mathbf{r}_{\text{cn}+}) \cdot \rho_{\text{cn}+} + \mathbf{A}_i(\mathbf{r}_{\text{cn}-}) \cdot \rho_{\text{cn}-} ] , \quad (8b)$$

$$\text{and, } \langle \mathbf{B}_n \cdot \nabla \Phi_i \rangle = - \langle (\nabla \cdot \mathbf{B}_n) \Phi_i \rangle = L_n [ \Phi_i(\mathbf{r}_{\text{cn}-}) - \Phi_i(\mathbf{r}_{\text{cn}+}) ] . \quad (8c)$$

This can be cast in the usual matrix notation as:  $[\mathbf{V}] = [\mathbf{Z}][\mathbf{I}]$ , where the elements of the matrix  $[\mathbf{V}]$  are:  $V_n = \langle \mathbf{E}^{\text{inc}} \cdot \mathbf{B}_n \rangle$ , and the elements of  $[\mathbf{Z}]$  are:  $Z_{ni} = \langle \mathbf{B}_n \cdot (j\omega \mathbf{A}_i) \rangle + \langle \mathbf{B}_n \cdot \nabla \Phi_i \rangle$ . The evaluation of  $V_n$  is straight-forward based on eqn. (8a). Hence, from a numerical implementation standpoint, the main task in the solution of the system of linear equations is the evaluation of the matrix elements  $Z_{ni}$ . The computation for  $Z_{ni}$  are discussed next.

## II.B Evaluation of the Matrix Elements :

Inspection of eqns. (8b) and (8c), reveals that the matrix elements  $Z_{ni}$  contain two types of terms:  $\mathbf{A}_i(\mathbf{r}_{\text{cn}}) \cdot \rho_{\text{cn}}$  and  $\Phi_i(\mathbf{r}_{\text{cn}})$ . The  $\mathbf{A}_i(\mathbf{r}_{\text{cn}}) \cdot \rho_{\text{cn}}$  terms require surface integrations  $I_1$  of the form:

$$I_1 \sim [L_i/(2A_i)] \{ \iint_{S'} (1/R) \exp[-jkR] \rho_i dS' \} , \quad (9a)$$

where  $R = |\mathbf{r}_{\text{cn}} - \mathbf{r}'|$ . Here,  $\mathbf{r}'$  is a source point in the  $i^{\text{th}}$  triangle,  $\rho_i$  the position vector from the vertex of the  $i^{\text{th}}$  triangle to the source point, and  $\mathbf{r}_{\text{cn}}$  the centroid of the  $n^{\text{th}}$  triangle. Similarly, all of the  $\Phi_i(\mathbf{r}_{\text{cn}})$  terms require surface integrations  $I_2$  of the form:

$$I_2 \sim [L_i/A_i] \{ \iint_{S'} (1/R) \exp[-jkR] dS' \} . \quad (9b)$$

If the  $n^{\text{th}}$  and  $i^{\text{th}}$  triangles are different (i.e. for  $n \neq i$ ), the value of  $R$  is always non-zero, and no singularity results. In such cases, the following methods can all be used for evaluating the triangular double integrals: (i) A one-point approximation by sampling at the centroid of the triangle. This is the least accurate method, but could suffice if  $R \gg R_{C \max}$ , with  $R_{C \max}$  being the maximum distance between the centroids of all the patches. (ii) Use of a seven-point numerical integration valid for triangular sources as given by Stroud [20]. (iii) A numerical integration technique based on the normalized area co-ordinates [21] as discussed by Rao et al. [19]. However, if  $i = n$ , then  $R$  can approach zero and the integrands become singular. For such situations, the singularity has to be removed by decomposing the integrals into an analytical and a numerical part as outlined in Ref. 18. Thus:

$$I_1 \sim \{ \iint_{S'} (1/R) \exp[-jkR] \rho_l dS' \} = \iint_{S'} (1/R) \{ \exp[-jkR] - 1 \} \rho_l dS' + \iint_{S'} (\rho_l/R) dS' , \quad (10a)$$

$$\text{and, } I_2 \sim \{ \iint_{S'} (1/R) \exp[-jkR] dS' \} = \iint_{S'} (1/R) \{ \exp[-jkR] - 1 \} dS' + \iint_{S'} (1/R) dS' , \quad (10b)$$

i.e.  $I_1 = I_{11} + I_{12}$ , and  $I_2 = I_{21} + I_{22}$ . Of the four integral terms on the right sides of eqns. (10a) and (10b),  $I_{11}$  and  $I_{21}$  can both be integrated numerically, since  $\lim_{R \rightarrow 0} [\{ \exp[-jkR] - 1 \} / R] \rightarrow -jk$ , and hence, the integrand is finite and non-divergent. The integrals  $I_{12}$  and  $I_{22}$  can be evaluated analytically [18, 21, 22], and the resulting expressions can best be understood in terms of Fig. 2 showing a planar triangle. In Fig. 2, the triangle is defined by a local reference frame  $(u, v, w)$  and assumed to lie in the  $w = 0$  plane. Each side of length  $L_i$  ( $i = 1, 2, 3$ ) is shown to be opposite node  $n_i$  with co-ordinates  $(0, 0, 0)$ ,  $(L_3, 0, 0)$  and  $(u_3, v_3, 0)$ . Also, as shown in Fig. 2,  $t_i^+$  and  $t_i^-$  are distances from the observation point  $(u_0, v_0, 0)$  to the end points of each side  $L_i$ . From a geometric analysis, one obtains :

$$s_1^- = - [(L_3 - u_0)(L_3 - u_3) + v_0 v_3] / L_1 , \quad (11a)$$

$$s_1^+ = [(u_3 - u_0)(u_3 - L_3) + v_3(v_3 - v_0)] / L_1 , \quad (11b)$$

$$s_2^- = - [u_3(u_3 - u_0) + v_3(v_3 - v_0)] / L_2 , \quad (11b)$$

$$s_2^+ = [u_0 u_3 + v_0 v_3] / L_2 , \quad (11d)$$

$$s_3^- = -u_0 , \text{ and } s_3^+ = L_3 - u_0 , \quad (11e) \quad t_1^- = [(L_3 - u_0)^2 + (v_3 - v_0)^2]^{0.5} , \quad (11f)$$

$$t_1^+ = [(u_3 - u_0)^2 + (v_3 - v_0)^2]^{0.5} , \quad (11g)$$

$$t_2^+ = [u_0^2 + v_0^2]^{0.5} , \quad (11h)$$

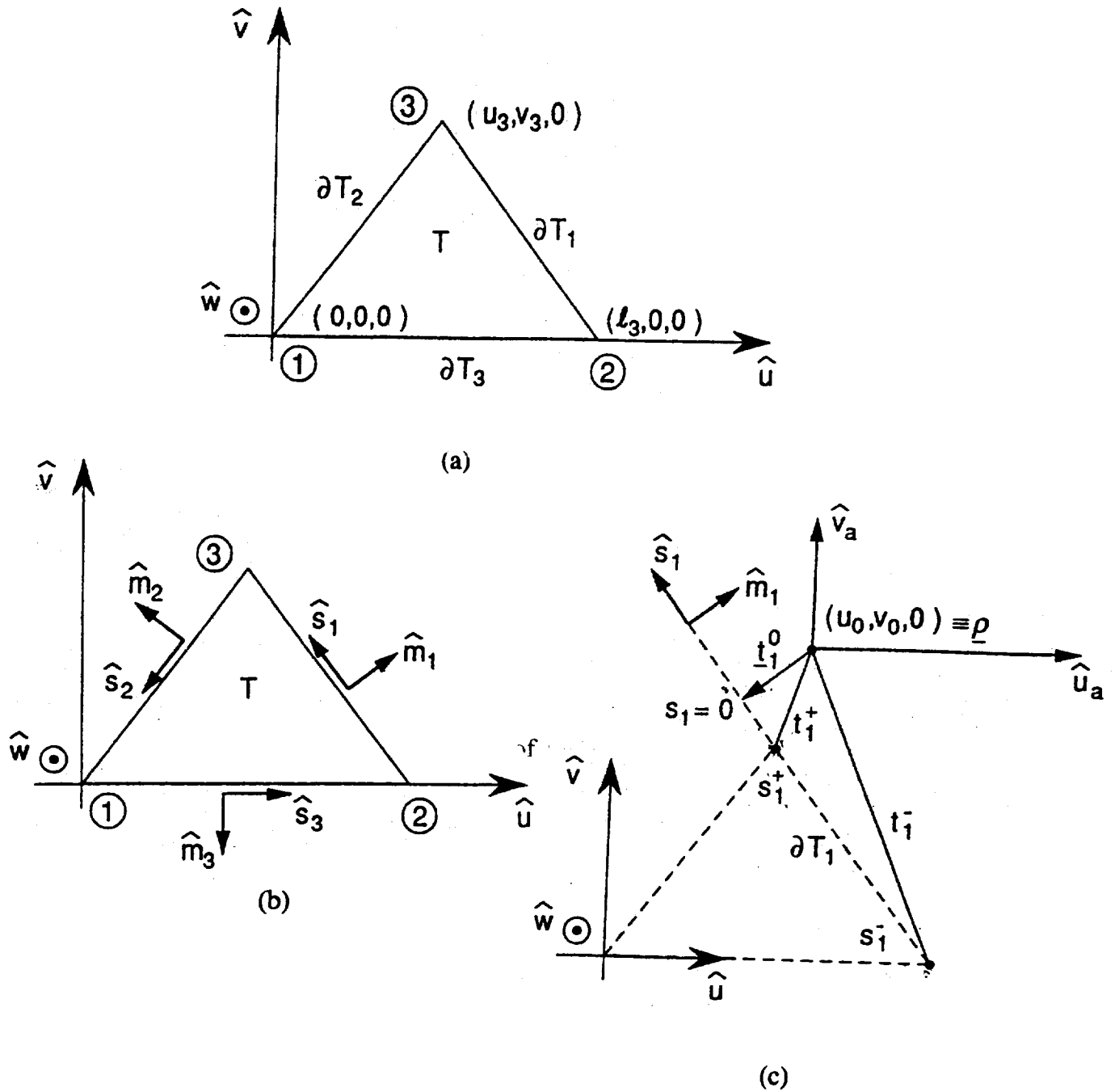


Fig. 2. Triangular geometry for the integral evaluations [after reference 22]. (a) Plane triangle  $T$  in its local frame ( $u, v, w = 0$ ). The length of the  $i^{\text{th}}$  side  $\partial T_i$  is denoted by  $L_i$ . (b) The tangent  $s^A$  and normal  $m^A$  unit vectors on the triangle contour. (c) The distances  $t_i$  and  $s_i$  defined in the text from the local point at  $(u_0, v_0, 0)$ .

$$t_3^+ = t_1^- ; t_2^- = t_1^+ ; t_3^- = t_2^+ , \quad (11i)$$

$$t_1^0 = v_0 [(u_3 - L_3) + v_3 (L_3 - u_0)] / L_1 , \quad (11j)$$

$$t_2^0 = [u_0 u_3 - v_0 u_3] / L_2 , \text{ and } t_3^0 = v_0 . \quad (11k)$$

In terms of the geometric parameters defined in eqn. (11a-11k), the integrals  $I_{12}$  and  $I_{22}$  are [18,22] :

$$I_{12} = \iint_{S'} ((\rho/R) dS' = \mathbf{I} + \rho_{cn} I_{22} , \quad (12a)$$

$$\text{where , } \mathbf{I} = 0.5 \sum_{i=1}^3 \mathbf{m}_i \{ (t_i^0)^2 \text{Ln} [\{t_i^+ + s_i^+\} / \{t_i^- + s_i^-\}] + t_i^+ s_i^+ - t_i^- s_i^- \} , \quad (12b)$$

$$\text{and , } I_{22} = \iint_{S'} (1/R) dS' = \sum_{i=1}^3 t_i^0 \text{Ln} [\{t_i^+ + s_i^+\} / \{t_i^- + s_i^-\}] . \quad (12c)$$

In eqn. (12b),  $\mathbf{m}_i$  are the outward unit normals from the lines opposite the  $i^{\text{th}}$  node as shown in Fig. 2.

### II.C Example of Incident Plane Wave for the Moment Method :

Incident excitation on the planar surface used for the MM above can have a variety of form depending on the source. These could include plane waves for scattering problems, delta-gap and magnetic frills for linear antenna sources, magnetic currents excitations for slot and aperture antennas. Here, for simplicity once again, an incident plane wave excitation has been chosen as a demonstrative example. Thus:  $\mathbf{E}^{\text{inc}}(\mathbf{r}) = [E_\theta \mathbf{a}_\theta + E_\phi \mathbf{a}_\phi] \exp[-j\mathbf{k} \cdot \mathbf{r}]$  , with  $\mathbf{a}_\theta$  and  $\mathbf{a}_\phi$  being unit vectors. In terms of Cartesian co-ordinates, these vectors can be expressed as:

$$\mathbf{a}_\theta = \cos\theta \cos\phi \mathbf{a}_x + \cos\theta \sin\phi \mathbf{a}_y - \sin\theta \mathbf{a}_z ; \quad \mathbf{a}_\phi = -\sin\phi \mathbf{a}_x + \cos\phi \mathbf{a}_y - \sin\theta \mathbf{a}_z , \quad (13a)$$

$$\text{and , } \mathbf{k} = |\mathbf{k}| [\sin\theta \cos\phi \mathbf{a}_x + \sin\theta \sin\phi \mathbf{a}_y + \cos\theta \mathbf{a}_z] . \quad (13b)$$

### III. Aspects of Physical Optics and the Hybrid MM-PO Scheme :

As already mentioned in the introduction section, the behavior of antennas (and radiators) installed on complex conducting structures (e.g. ships, aircrafts, etc..) are modified with respect to

free-space operation due to the interactions between each antenna and the supporting structure. The development of numerical methods for estimating the interactions between on-board antennas and arbitrary-shaped, on-board, sub-structures is of great interest for electromagnetic compatibility control. This includes the overall performance evaluation and control of all on-board radiating systems, electromagnetic interference, and personnel radiation hazards.

Since the MM is computationally intensive and hence, limits the size of objects that can be modeled, hybrid techniques that combine the MM with other approximate solutions have begun to receive attention [10,11,23]. These can be classified as either ray-based [8,9,24] or current-based [14-16,25,26] techniques. Of these, the ray-based techniques provide a considerable speed advantage, but are difficult to implement for arbitrary geometries and complex objects. By contrast, the current-based methods, in which one attempts to determine equivalent surface currents that represent the actual objects, are capable of modeling irregular and complex geometries.

Here, the focus is on time-harmonic problems in which a large perfectly electric conducting (PEC) body (e.g. aircraft) has a set of on-board antennas on its surface. This basic problem can be replaced by an equivalent problem in which the PEC surface is replaced by equivalent currents radiating in space. In the *simplest* sense, the problem reduces to obtaining the surface currents  $\mathbf{J}$  induced by the excitation fields ( $\mathbf{E}^{\text{inc}}$ ,  $\mathbf{H}^{\text{inc}}$ ). Since current based MM scheme is computationally intensive, a possible solution being attempted here is the use of an alternate hybrid method that combines physical optics (PO) with the MM approach. This could be done by dividing the overall surface into an MM zone (MMZ) which can be used over any part of the given geometry, but is most essential over irregular and “non-smooth” geometries, and the remaining PO sub-region (POSR). As discussed in the preceding section, the current  $\mathbf{J}$  over the MMZ would be given as:  $\mathbf{J} = \sum_1^N \mathbf{I}_i \mathbf{B}_i(\mathbf{r})$ . Based on the coefficients  $\mathbf{I}_i$  (obtained from a MM solution over MMZ), the scattered E-field could be evaluated using eqn. (6). Such a *simple* solution, however, would include only the coupling between the source radiation and the MMZ, and would *not contain any interactions with the POSR*.

The computational scheme being proposed for use here would couple the MM and the POSR to include mutual interactions. It is similar to the hybrid methods that have been proposed by Hodges and Rahmat-Samii [16] and Obelleiro et al. [27]. Let  $\mathbf{J}_1$  and  $\mathbf{J}_2$  represent the surface currents across the MMZ and the POSR sub-domains, respectively. Quite generally, the electric-field integral equation (EFIE) can be applied to the MMZ with  $\mathbf{J}_2$  taken to be an effective source current, while the magnetic-field integral equation (MFIE) applied to POSR with  $\mathbf{J}_2$  as the source current. This leads to

the following system of coupled equations [16] :

$$\mathbf{L}_e[\mathbf{J}_1(\mathbf{r})] + \mathbf{L}_e[\mathbf{J}_2(\mathbf{r})] = -\mathbf{E}_{\text{tan}}^{\text{inc}}(\mathbf{r}) , \quad \text{for } \mathbf{r} \in \text{MMZ} \quad (14a)$$

$$\text{and, } \mathbf{J}_2(\mathbf{r}) = 2 \mathbf{n}^\wedge \times \mathbf{H}^{\text{inc}}(\mathbf{r}) + \mathbf{L}_h[\mathbf{J}_1(\mathbf{r})] + \mathbf{L}_h[\mathbf{J}_2(\mathbf{r})] , \quad \text{for } \mathbf{r} \in \text{POSR} \quad (14b)$$

where  $\mathbf{n}^\wedge$  is the unit surface normal, and the operators  $\mathbf{L}_e[\mathbf{J}(\mathbf{r})]$  and  $\mathbf{L}_h[\mathbf{J}(\mathbf{r})]$  are defined as :

$$\mathbf{L}_e[\mathbf{J}(\mathbf{r})] = -j\omega\mathbf{A}(\mathbf{r}) - \nabla\Phi(\mathbf{r}) = -j\omega \mu \iint_{S'} \mathbf{J}(\mathbf{r}') G(\mathbf{r}, \mathbf{r}') dS' + \{1/(j\omega\epsilon)\} \nabla \iint_{S'} \nabla' \cdot \mathbf{J}(\mathbf{r}') G(\mathbf{r}, \mathbf{r}') dS' , \quad (14c)$$

$$\text{and, } \mathbf{L}_h[\mathbf{J}(\mathbf{r})] = 2 \mathbf{n}^\wedge \times \iint_{S'} \mathbf{J}(\mathbf{r}') \times [\nabla' G(\mathbf{r}, \mathbf{r}')] dS' , \quad (14d)$$

$$\text{with } G(\mathbf{r}, \mathbf{r}') = \{\exp[-j k |\mathbf{r} - \mathbf{r}'|]\} / \{4 \pi |\mathbf{r} - \mathbf{r}'|\} . \quad (14e)$$

Eqn. (14b) is complete, yet quite complicated since the current  $\mathbf{J}_2(\mathbf{r})$  has three components – (i) the  $\mathbf{n}^\wedge \times \mathbf{H}^{\text{inc}}(\mathbf{r})$  term originates includes the surface currents induced by the incident magnetic field (due to the true sources), (ii) a  $\mathbf{L}_h[\mathbf{J}_1(\mathbf{r})]$  term that arises from the mutual interaction effect of currents  $\mathbf{J}_1(\mathbf{r})$  flowing in the MMZ. Such MMZ currents give rise to a scattered electric field, which in turn can induce a current component in the POSR, and (iii) the  $\mathbf{L}_h[\mathbf{J}_2(\mathbf{r})]$  term which denotes self-induction contributions. These are the currents induced in the POSR due to currents already flowing within this region.

For a PO implementation, the following approximations are made for simplicity :

- (i) The first term of eqn. (14b) is taken to equal:  $2 \mathbf{n}^\wedge \times \mathbf{H}^{\text{inc}}(\mathbf{r})$  in the “lit” or “directly illuminated” parts of the POSR, and is set to zero over the “shadow” sub-sections. The PO approach uses the following approximation for current  $\mathbf{J}$  on a conducting surface with an incident magnetic field  $\mathbf{H}_i$  and unit normal  $\mathbf{n}^\wedge$  :  $\mathbf{J} = 2 \gamma \mathbf{n}^\wedge \times \mathbf{H}_i$  where  $\gamma$  is a coefficient that accounts for shadow effects. For observation points  $\mathbf{r}$  lying in the shadow region,  $\gamma = 0$  and  $\gamma = 1$  otherwise. Thus, it is



inherently assumed that edge-diffraction and multiple-scattering effects are negligible. Clearly, this would be an excellent approximation for surfaces that were large and relatively “flat” .

(ii) Next, the PO implementation assumes that self-induced currents can be neglected in comparison to those arising from the direct incident excitation and mutual-coupling from the MMZ. Consequently, the  $\mathbf{L}_h[\mathbf{J}_2(\mathbf{r})]$  term is set to zero, and one effectively obtains the following approximation:

$$\mathbf{J}_2(\mathbf{r}) \sim 2 \mathbf{n}^\wedge \times \mathbf{H}^{\text{inc}}(\mathbf{r}) + \mathbf{L}_h[\mathbf{J}_1(\mathbf{r})] , \quad \text{for } \mathbf{r} \in \text{“lit portion of POSR”} \quad (14f)$$

$$\mathbf{J}_2(\mathbf{r}) \sim \mathbf{L}_h[\mathbf{J}_1(\mathbf{r})] , \quad \text{for } \mathbf{r} \in \text{“dark/shadow portion of POSR”} . \quad (14g)$$

The resulting coupled system of equations to be solved in the hybrid MM-PO scheme are thus given by eqn. (14a), eqn. (14c), and eqn. (14f-g). Since the incident source field is always specified in any problem, the only unknowns involve the currents  $\mathbf{J}_1(\mathbf{r})$  over the MMZ. These can be solved using the MM matrix procedure outlined in the previous section. Consequently, the overall solution process does not become any more complicated than that for the MM. Thus, by choosing as small an MMZ as possible (i.e., including only the irregular or complex geometric portions, or the near-field regions), the computational requirement can be greatly reduced.

### III.A Matrix Elements for the Hybrid MM-PO Scheme :

As with the previous discussion on the MM implementation, the relevant matrix equations for the hybrid MM-PO scheme are given here for a simple surface geometry, neglecting any wires, wire-surface and wire-wire interactions. In general, the MM could be applied to all wire sections, and hence, all wires and wire-sections included in the MMZ. Using the surface basis functions  $\mathbf{B}_n(\mathbf{r})$  as given in eqn. (5), the appropriate matrix elements for the hybrid scheme can be obtained. The details are given next.

Using  $\mathbf{J}_1(\mathbf{r}) = \sum_1^N \mathbf{I}_l(\mathbf{r}) \mathbf{B}_l(\mathbf{r})$ , eqn. (14a) can be re-written with the aid of eqn. (14c) as:

$$\begin{aligned} -j\omega \mu \iint_{\text{SMM}} \{ \sum_1^N \mathbf{I}_l(\mathbf{r}') \mathbf{B}_l(\mathbf{r}') \} G(\mathbf{r}, \mathbf{r}') d\mathbf{S}' + \{ 1/(j\omega\epsilon) \} \nabla \cdot \{ \sum_1^N \mathbf{I}_l(\mathbf{r}') \mathbf{B}_l(\mathbf{r}') \} G(\mathbf{r}, \mathbf{r}') d\mathbf{S}' + \\ + \mathbf{L}_e[\mathbf{J}_2(\mathbf{r})] = -\mathbf{E}^{\text{inc}}_{\text{tan}}(\mathbf{r}) , \quad \text{for } \mathbf{r} \in \text{MMZ} \end{aligned} \quad (15a)$$

where the surface integrals are over the MMZ. Hence, the inner product  $\langle \mathbf{E}_{\text{tan}}^{\text{inc}}(\mathbf{r}) \cdot \mathbf{B}_n(\mathbf{r}) \rangle$  can be expressed as the sum of three terms i.e.,  $\langle \mathbf{E}_{\text{tan}}^{\text{inc}}(\mathbf{r}) \cdot \mathbf{B}_n(\mathbf{r}) \rangle = T_{1n} + T_{2n} + T_{3n}$ , where :

$$\langle \mathbf{E}_{\text{tan}}^{\text{inc}}(\mathbf{r}) \cdot \mathbf{B}_n(\mathbf{r}) \rangle = (L_n/2) [ \mathbf{E}^{\text{inc}}(\mathbf{r}_{\text{cn}+}) \cdot \rho_{\text{cn}+} + \mathbf{E}^{\text{inc}}(\mathbf{r}_{\text{cn}-}) \cdot \rho_{\text{cn}-} ] , \quad (\text{from 8a})$$

$$T_{1n} = j\omega \mu \langle \mathbf{B}_n(\mathbf{r}) \cdot \iint_{\text{SMM}} \{ \sum_1^N \mathbf{I}_l(\mathbf{r}') \mathbf{B}_l(\mathbf{r}') \} G(\mathbf{r}, \mathbf{r}') d\mathbf{S}' \rangle , \quad (15b)$$

$$T_{2n} = - \{ 1/(j\omega\epsilon) \} \langle \mathbf{B}_n(\mathbf{r}) \cdot \nabla \iint_{\text{SMM}} \nabla' \cdot \{ \sum_1^N \mathbf{I}_l(\mathbf{r}') \mathbf{B}_l(\mathbf{r}') \} G(\mathbf{r}, \mathbf{r}') d\mathbf{S}' \rangle , \quad (15c)$$

$$T_{3n} = - \langle \mathbf{B}_n(\mathbf{r}) \cdot \mathbf{L}_e[\mathbf{J}_2(\mathbf{r})] \rangle . \quad (15d)$$

Expressions for the three terms  $T_{1n}$ ,  $T_{2n}$  and  $T_{3n}$  can now be worked out. Thus:

$$T_{1n} = \sum_1^N \mathbf{I}_l \{ (j\omega L_n/2) [ \mathbf{A}_l(\mathbf{r}_{\text{cn}+}) \cdot \rho_{\text{cn}+} + \mathbf{A}_l(\mathbf{r}_{\text{cn}-}) \cdot \rho_{\text{cn}-} ] \} , \quad (15e)$$

$$T_{2n} = \sum_1^N \mathbf{I}_l L_n [ \Phi_l(\mathbf{r}_{\text{cn}-}) - \Phi_l(\mathbf{r}_{\text{cn}+}) ] , \quad (15f)$$

$$T_{3n} = - \langle \mathbf{B}_n(\mathbf{r}) \cdot \{ -j\omega \mu \iint_{\text{S}} \mathbf{J}_2(\mathbf{r}') G(\mathbf{r}, \mathbf{r}') d\mathbf{S}' + \{ 1/(j\omega\epsilon) \} \nabla \iint_{\text{S}} \nabla' \cdot \mathbf{J}_2(\mathbf{r}') G(\mathbf{r}, \mathbf{r}') d\mathbf{S}' \} \rangle , \quad (15g)$$

where the surface integration for  $T_{3n}$  is over the POSR. The terms  $T_{1n}$  and  $T_{2n}$  are the same as obtained before in eqn. (8b) and (8c). Using eqns. (14f) and (14g), the  $T_{3n}$  expression can be split

into two parts  $T_{3n1}$  and  $T_{3n2}$  with  $T_{3n1}$  containing the  $2 \mathbf{n}^\wedge \times \mathbf{H}^{\text{inc}}(\mathbf{r})$  factor, and  $T_{3n2}$  the  $\mathbf{L}_h[\mathbf{J}_1(\mathbf{r})]$  term. In turn,  $T_{3n1}$  will have two terms due to the two integrals inherent in eqn. (15g). Expressing  $T_{3n1} = T_{3n1A} + T_{3n1B}$  to denote the two terms, one has :

$$T_{3n1} = T_{3n1A} + T_{3n1B} = - \langle \mathbf{B}_n(\mathbf{r}) \cdot \{ -j\omega \mu \iint_{\text{SPO}} \{ 2 \mathbf{n}^\wedge \times \mathbf{H}^{\text{inc}}(\mathbf{r}') \} G(\mathbf{r}, \mathbf{r}') d\mathbf{S}' \} -$$

$$- \langle \mathbf{B}_n(\mathbf{r}) \cdot \{ 1/(j\omega\epsilon) \} \nabla \iint_{\text{SPO}} \nabla' \cdot \{ 2 \mathbf{n}^\wedge \times \mathbf{H}^{\text{inc}}(\mathbf{r}') \} G(\mathbf{r}, \mathbf{r}') d\mathbf{S}' \} \rangle . \quad (15h)$$

Hence,

$$T_{3n1A} = \{ j\omega L_n \mu / (4\pi) \} [ \rho_{n+}(\mathbf{r}_{\text{cn}+}) \cdot \Delta \mathbf{V}_{n1+} + \rho_{n-}(\mathbf{r}_{\text{cn}-}) \cdot \Delta \mathbf{V}_{n1-} ] , \quad (15i)$$

$$\text{where } \Delta \mathbf{V}_{n1\pm} = \{ \int \int_{\text{SPO}} \{ \mathbf{n}^{\wedge} \times \mathbf{H}^{\text{inc}}(\mathbf{r}') \} \exp(-jk|\mathbf{r}_{\text{cn}\pm} - \mathbf{r}'|) / (|\mathbf{r}_{\text{cn}\pm} - \mathbf{r}'|) d\mathbf{S}' \} . \quad (15j)$$

Similarly, for  $T_{3n1B}$  one gets :

$$T_{3n1B} = \{ -L_n / (j4\pi\omega\epsilon) \} [ \rho_{n+}(\mathbf{r}_{\text{cn}+}) \cdot \Delta \mathbf{V}_{n2+} + \rho_{n-}(\mathbf{r}_{\text{cn}-}) \cdot \Delta \mathbf{V}_{n2-} ] , \quad (15k)$$

$$\text{where } \Delta \mathbf{V}_{n2\pm} = \nabla \{ \int \int_{\text{SPO}} \nabla' \cdot \{ \mathbf{n}^{\wedge} \times \mathbf{H}^{\text{inc}}(\mathbf{r}') \} \exp(-jk|\mathbf{r}_{\text{cn}\pm} - \mathbf{r}'|) / (|\mathbf{r}_{\text{cn}\pm} - \mathbf{r}'|) d\mathbf{S}' \} . \quad (15l)$$

Thus, both the  $T_{3n1A}$  and  $T_{3n1B}$  terms do *not* depend on the unknown coefficients  $I_i$ . Next, from eqn. (15g), the  $T_{3n2}$  term has the form :

$$\begin{aligned} T_{3n2} &= T_{3n2A} + T_{3n2B} = - < \mathbf{B}_n(\mathbf{r}) \cdot \{ -j\omega \mu \int \int_{\text{SPO}} \{ \mathbf{L}_h[\mathbf{J}_1(\mathbf{r})] \} G(\mathbf{r}, \mathbf{r}') d\mathbf{S}' \} > - \\ &- < \mathbf{B}_n(\mathbf{r}) \cdot \{ 1/(j\omega\epsilon) \} \nabla \int \int_{\text{SPO}} \nabla' \cdot \{ \mathbf{L}_h[\mathbf{J}_1(\mathbf{r})] \} G(\mathbf{r}, \mathbf{r}') d\mathbf{S}' \} > . \quad (15m) \end{aligned}$$

Using the expansion  $\mathbf{J}_1(\mathbf{r}) = \sum_{i=1}^N \mathbf{I}_i \mathbf{B}_i(\mathbf{r})$ , the  $T_{3n2A}$  and  $T_{3n2B}$  factors can each be cast as an appropriate summation over  $N$  weighted by the unknown coefficients  $I_i$ . Thus:

$$\begin{aligned} T_{3n2A} &= \sum_{i=1}^N (I_i j\omega \mu L_n) \{ [\rho_{n++} \int \int_{\text{SPO}} \{ \mathbf{n}^{\wedge} \times \int \int_i \mathbf{B}_i(\mathbf{r}'') \times \nabla' G(\mathbf{r}', \mathbf{r}'') d\mathbf{S}'' \} G(\mathbf{r}, \mathbf{r}') d\mathbf{S}' ] + \\ &+ [\rho_{n--} \int \int_{\text{SPO}} \{ \mathbf{n}^{\wedge} \times \int \int_i \mathbf{B}_i(\mathbf{r}'') \times \nabla' G(\mathbf{r}', \mathbf{r}'') d\mathbf{S}'' \} G(\mathbf{r}, \mathbf{r}') d\mathbf{S}' ] , \quad (15n) \end{aligned}$$

where the innermost integral is over the two triangles  $T_{i\pm}$  in MMZ, and the outer integral is over the entire POSR. Assuming that the MMZ and POSR are well separated so that the one-point formula can be used as an approximation for the surface integral, one gets from eqn. (15n) :

$$T_{3n2A} = \sum_{i=1}^N \{ (I_i j\omega \mu L_n L_i) / (32\pi^2) \} [ \rho_{n++} \cdot \mathbf{c}_{i+} + \rho_{n++} \cdot \mathbf{c}_{i-} + \rho_{n--} \cdot \mathbf{c}_{i+} + \rho_{n--} \cdot \mathbf{c}_{i-} ] , \quad (15o)$$

$$\text{with } \mathbf{c}_{i\pm} = \int \int_{\text{SPO}} \{ \mathbf{n}^{\wedge} \times \rho_{i\pm}(\mathbf{r}_{\text{ci}\pm}) \times \nabla' [ \exp(-jk|\mathbf{r}' - \mathbf{r}_{\text{ci}\pm}|) / |\mathbf{r}' - \mathbf{r}_{\text{ci}\pm}| ] \} \exp(-jk|\mathbf{r}_{\text{cn}} - \mathbf{r}'|) / |\mathbf{r}_{\text{cn}} - \mathbf{r}'| d\mathbf{S}' , \quad (15p)$$

Similarly, one obtains for  $T_{3n2B}$  :

$$T_{3n2B} = \frac{1}{\sum} \{-(\mathbf{I}_1 L_n L_i)/(32\pi^2 j\omega\epsilon)\} [\rho_{n++} \cdot \mathbf{d}_{i+} + \rho_{n++} \cdot \mathbf{d}_{i-} + \rho_{n--} \cdot \mathbf{d}_{i+} + \rho_{n--} \cdot \mathbf{d}_{i-}] , \quad (15q)$$

$$\mathbf{d}_{i\pm} = \nabla \int \int_{SPO} \nabla' \cdot \{\mathbf{n}^\wedge \times \rho_{i\pm}(\mathbf{r}_{ci\pm}) \times \nabla' [\exp(-jk|\mathbf{r}' - \mathbf{r}_{ci\pm}|) / |\mathbf{r}' - \mathbf{r}_{ci\pm}|] \} \exp(-jk|\mathbf{r}_{cn} - \mathbf{r}'|) / |\mathbf{r}_{cn} - \mathbf{r}'| \} dS' , \quad (15r)$$

Putting together the  $T_{1n}$ ,  $T_{2n}$ ,  $T_{3n1A}$ ,  $T_{3n1B}$ ,  $T_{3n2A}$  and  $T_{3n2B}$  terms a composite matrix equation of the form  $[V + \delta V] = [Z + \delta Z] \cdot [I]$ , i.e.  $[V^*] = [Z^*] \cdot [I]$  results. Using the following notation for compactness:

$$P_n = (L_n/2) [ \mathbf{E}^{inc}(\mathbf{r}_{cn+}) \cdot \rho_{cn+} + \mathbf{E}^{inc}(\mathbf{r}_{cn-}) \cdot \rho_{cn-} ] , \quad (16a)$$

$$Q_n = \{j\omega L_n \mu/(4\pi)\} [ \rho_{n+}(\mathbf{r}_{cn+}) \cdot \Delta \mathbf{V}_{n1+} + \rho_{n-}(\mathbf{r}_{cn-}) \cdot \Delta \mathbf{V}_{n1-} ] , \quad (16b)$$

$$R_n = \{-L_n/(j4\pi\omega\epsilon)\} [ \rho_{n+}(\mathbf{r}_{cn+}) \cdot \Delta \mathbf{V}_{n2+} + \rho_{n-}(\mathbf{r}_{cn-}) \cdot \Delta \mathbf{V}_{n2-} ] , \quad (16c)$$

$$S_{ni} = \{(j\omega L_n/2) [ \mathbf{A}_i(\mathbf{r}_{cn+}) \cdot \rho_{cn+} + \mathbf{A}_i(\mathbf{r}_{cn-}) \cdot \rho_{cn-} ] \} , \quad (16d)$$

$$T_{ni} = L_n [ \Phi_i(\mathbf{r}_{cn-}) - \Phi_i(\mathbf{r}_{cn+}) ] , \quad (16e)$$

$$U_{ni} = \{(j\omega \mu L_n L_i)/(32\pi^2)\} [ \rho_{n++} \cdot \mathbf{c}_{i+} + \rho_{n++} \cdot \mathbf{c}_{i-} + \rho_{n--} \cdot \mathbf{c}_{i+} + \rho_{n--} \cdot \mathbf{c}_{i-} ] , \quad (16f)$$

$$V_{ni} = \{-(L_n L_i)/(32\pi^2 j\omega\epsilon)\} [ \rho_{n++} \cdot \mathbf{d}_{i+} + \rho_{n++} \cdot \mathbf{d}_{i-} + \rho_{n--} \cdot \mathbf{d}_{i+} + \rho_{n--} \cdot \mathbf{d}_{i-} ] , \quad (16g)$$

one has :

$$[V + \delta V]_n = [V^*]_n = [P_n + Q_n + R_n] , \quad (16h)$$

$$\text{and } [Z + \delta Z]_{ni} = [Z^*]_{ni} = [S_{ni} + T_{ni} + U_{ni} + V_{ni}] . \quad (16i)$$

Solution of the modified matrix  $[V^*] = [Z^*] [I]$ , then yields the unknown coefficients  $[I]$  as before, but with much less computational burden.

#### IV. The Finite-Difference, Time-Domain (FDTD) Method

The finite-difference, time-domain (FDTD) technique, was first proposed by Yee [28] as a

numerical method for the direct solution of Maxwell's time-dependent curl equations. Its popularity continues to grow as the computational costs decline. The Maxwell's curl equations are [29]:

$$\begin{aligned}\frac{\partial \vec{E}}{\partial t} &= \frac{1}{\epsilon} \nabla \times \vec{H} - \frac{\sigma}{\epsilon} \vec{E} \\ \frac{\partial \vec{H}}{\partial t} &= -\frac{1}{\mu} \nabla \times \vec{E} - \frac{\rho'}{\mu} \vec{H}\end{aligned}, \quad (17)$$

where  $\sigma$  is electrical conductance;  $\rho'$  the magnetic conductance is zero for the present problem.

In this method, the electric (E) and magnetic (H) fields are discretized across separate nodes that are off by half a grid spacing. The time instants at which the E and H fields are updated are also off by half a time step. The discretization of the Maxwell curl equations results in six explicit finite difference equations [30]. For example, for a two-dimensional (2D) transverse magnetic case, the z component of the electric field  $E_z$  and y component of the magnetic field  $H_y$  are given as :

$$E_z^{n+1}(i, j) = \left( \frac{1 - \frac{\sigma_{i,j} \Delta t}{2\epsilon_{i,j}}}{1 + \frac{\sigma_{i,j} \Delta t}{2\epsilon_{i,j}}} \right) E_z^n(i, j) + \frac{\frac{\Delta t}{\epsilon_{i,j}}}{1 + \frac{\sigma_{i,j} \Delta t}{2\epsilon_{i,j}}} \left[ \frac{H_y^{n+1/2}(i, j) - H_y^{n+1/2}(i-1, j)}{\Delta x} - \frac{H_x^{n+1/2}(i, j) - H_x^{n+1/2}(i, j-1)}{\Delta y} \right] \quad (18a)$$

$$H_x^{n+1/2}(i, j) = H_x^{n-1/2}(i, j) - \frac{\Delta t}{\mu} \left[ \frac{E_z^n(i, j+1) - E_z^n(i, j)}{\Delta y} \right], \quad (18b)$$

$$\text{and, } H_z^{n+1/2}(i, j) = H_z^{n-1/2}(i, j) - \frac{\Delta t}{\mu} \left[ \frac{E_x^n(i+1, j) - E_x^n(i, j)}{\Delta x} \right]. \quad (18c)$$

In eqns. (18),  $\Delta x$  and  $\Delta y$  are grid spacings along the x and y directions, respectively, while  $\Delta t$  is the time step. The six finite-difference equations are stepped in time, alternately updating the electric and magnetic field components at each grid point. The value of  $\sigma_{i,j}$  is about  $10^{-2} \sim 10^{-3}$  and

$\Delta x = \Delta y = 10^{-8} \text{m}$  has been used here, so that:  $\frac{\sigma_{i,j} \Delta t}{2\epsilon_{i,j}} \ll 1$ . This condition simplifies eqn.(18a) to:

$$E_z^{n+1}(i, j) = E_z^n(i, j) + \frac{\Delta t}{\epsilon_{i,j}} \left[ \frac{H_y^{n+1/2}(i, j) - H_y^{n+1/2}(i-1, j)}{\Delta x} - \frac{H_x^{n+1/2}(i, j) - H_x^{n+1/2}(i, j-1)}{\Delta y} \right]. \quad (18d)$$

This FDTD method is well suited for solving the cellular scattering problem since the

leapfrog method leads to a second-order accuracy in both time and space. Furthermore, the following Courant criterion as suggested for Yee's algorithm was implemented to guarantee accuracy and stability [29] :

$$v_{\max} \cdot \Delta t \leq \frac{1}{\sqrt{\frac{1}{\Delta x^2} + \frac{1}{\Delta y^2} + \frac{1}{\Delta z^2}}} , \quad (19)$$

where  $v_{\max}$  is the maximum signal phase velocity in the configuration being considered. If the value of one of  $\Delta x$  and  $\Delta t$  is known or assigned, the value of other one can then be obtained.

Due to finiteness of the region used in any numerical simulation, care has to be taken to avoid artificial back-reflections from the simulation boundaries. Appropriate absorbing boundary conditions have to be implemented to ensure that unrealistic and unphysical wave reflections do not introduce spurious energy within the simulation region. A variety of boundary conditions have been reported [31] to prevent artificial reflections at the edges of the computational domain. These are either based on the solution of the wave equation [32,33], or the use of absorbing layers [30]. The Berenger approach [30] of using a perfectly matched layer (PML) provides orders of magnitude improvement in performance relative to the other techniques [29], and so has been implemented here. Since the wave decays very rapidly in the PML material of only a few layers ( $\sim 10$ ), exponential time-stepping has been used instead of the usual Yee time-stepping. This changes equation (17) within the PML to:

$$E_{zx}^{n+1}(i, j) = e^{-\sigma_x(i)\Delta t/\epsilon} E_{zx}^n - \frac{(1 - e^{-\sigma_x(i)\Delta t/\epsilon})}{\sigma_x(i)\Delta x} [-H_y^n(i+1/2, j) + H_y^n(i-1/2, j)] , \quad (20a)$$

$$E_{zy}^{n+1}(i, j) = e^{-\sigma_y(j)\Delta t/\epsilon} E_{zy}^n - \frac{(1 - e^{-\sigma_y(j)\Delta t/\epsilon})}{\sigma_y(j)\Delta y} [-H_x^n(i, j+1/2) + H_x^n(i, j-1/2)] , \quad (20b)$$

$$H_x^{n+1}(i+1/2, j) = e^{-\sigma_y^*(j+1/2)\Delta t/\mu} H_x^n(i+1/2, j) + \frac{(1 - e^{-\sigma_y^*(j+1/2)\Delta t/\mu})}{\sigma_y^*(j+1/2)\Delta y} \times \{E_{zx}^n(i, j+1) + E_{zy}^n(i, j+1) - [E_{zx}^n(i, j) + E_{zy}^n(i, j)]\} , \quad (20c)$$

$$H_y^{n+1}(i+1/2, j) = e^{-\sigma_x^*(i+1/2)\Delta t/\mu} H_y^n(i+1/2, j) + \frac{(1 - e^{-\sigma_x^*(i+1/2)\Delta t/\mu})}{\sigma_x^*(i+1/2)\Delta x} \times \{E_{zx}^n(i+1, j) + E_{zy}^n(i+1, j) - [E_{zx}^n(i, j) + E_{zy}^n(i, j)]\} . \quad (20d)$$

In the above,  $\sigma$  and  $\sigma^*$  are the electric and magnetic conductivities, respectively, and both are functions of the grid position index  $i$  and  $j$ . Component  $E_z$  is divided into  $E_{zx}$  and  $E_{zy}$  in the PML for TM case. In the computation region, the traditional discretizations for the curl functions 18(a-c) are used. If the impedance of the PML medium equals that of the material used in the computation region, then no reflection occur at the interface of these two materials. An essential conditional requirement is:

$$\frac{\sigma}{\epsilon_{cr}} = \frac{\sigma^*}{\mu_{cr}} \quad (21)$$

The index "cr" denotes the computation region, and  $\epsilon_0$  and  $\mu_0$  are used if the computation domain is air or a vacuum.

One of the advantages of this time domain method is that both narrow- and broad-band source excitations can easily be obtained. For broad-band pulse signals, a discrete Fourier transform (DFT) of the transient behavior yields the complete frequency response. The discrete Fourier transform, taken at every time-step of the simulation, is expressed by eqn. (22) below:

$$G(k\Delta f) = \Delta t \sum_{n=0}^{N_f-1} g(n\Delta t) \exp\left(\frac{-j2\pi kn}{N_f}\right) \quad , \quad \text{with} \quad k = 0, 1, 2, \dots, N_f \quad (22)$$

where  $G(k\Delta f)$  is the complex frequency domain data,  $g(n\Delta t)$  are the time domain E and H fields,  $N_f$  is the length of the DFT,  $\Delta f$  is the frequency step, and  $N_f$  represents the number of frequencies  $N_f = 1/(\Delta f \Delta t)$ .

Due to the computational limitations, a relatively small simulation domain is chosen for obtaining the fields from the FDTD method. This region closely surrounds the cell, and so, only the near-field distributions are directly obtained. Far field information on the intensity and phase can be obtained from the near-field E and H values based on the free-space Green's function and an integration procedure over a surface surrounding the cell [34,35]. In this procedure, the radiated E and H fields (in the frequency domain) tangential to a virtual surface completely surrounding the cell are converted into equivalent electric and magnetic surface current densities,  $J_{eq}$  and  $M_{eq}$ . These are then weighted by the Green's function and finally integrated to provide the desired far-field response. The current densities  $J_{eq}$  and  $M_{eq}$  can be obtained as:

$$\vec{J}_{eq}(r', \omega) = \hat{n} \times \vec{H}(r', \omega) \quad (23a)$$

$$\vec{M}_{eq}(r', \omega) = -\hat{n} \times \vec{E}(r', \omega) \quad (23b)$$

where  $r'$  is point on the virtual surface and  $\hat{n}$  is a unit vector normal to the surface.  $\vec{H}$  and  $\vec{E}$  are obtained by averaging the nearest components around the grid point on the virtual surface. For example, in the 2D case, the far-field is produced by equivalent electric and magnetic currents that are tangential to the non-physical virtual contour as shown in Fig. 3. The figure shows the overall geometric schematic that can be used for the simulations. The cell is shown in the center, with the electromagnetic wave incident from the left. The PML surrounds the simulation region completely on the periphery. Two contours, one for the near-to-far field transformation, and the other for evaluations of the total and scattering fields have also been shown in Fig. 3. On the left edge of the virtual contour for the near-to-far field transformation,  $\vec{E}(i+1/2, j)$  and  $\vec{H}(i, j)$  are obtained by:

$$\vec{E}(i, j+1/2) = [\vec{E}(i, j) + \vec{E}(i, j+1)]/2 \quad (24a)$$

$$\vec{H}(i+1/2, j) = [\vec{H}(i, j) + \vec{H}(i+1, j)]/2 \quad (24b)$$

The scattered electrical field in the far field region is given by [36] :

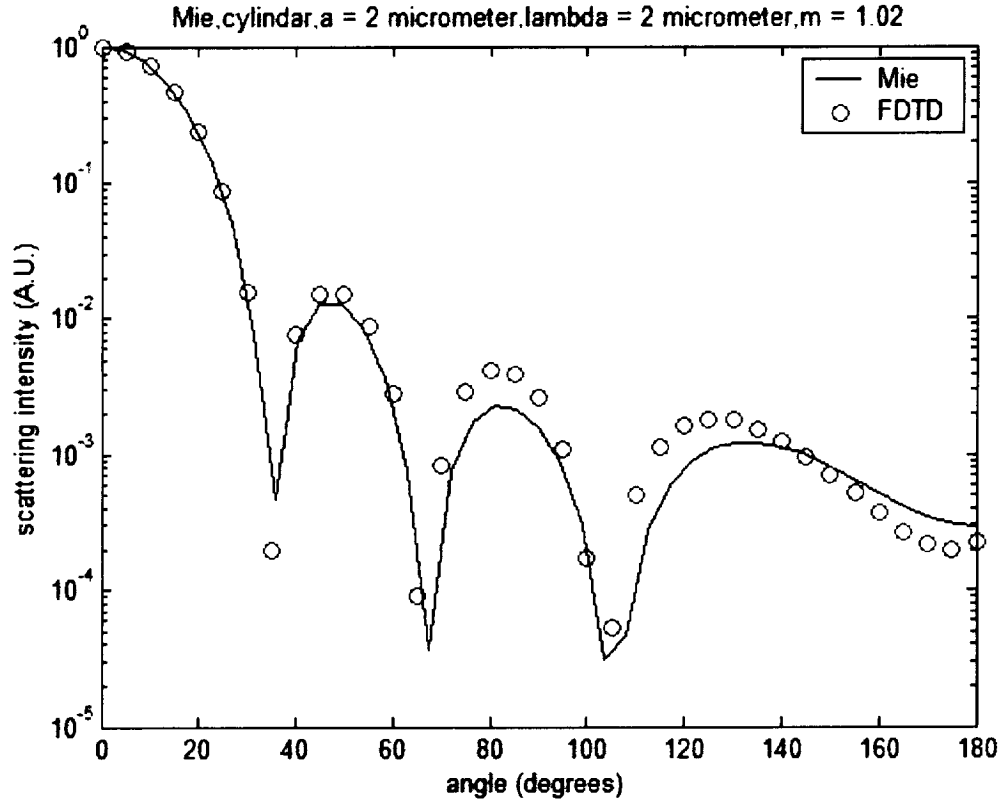


Fig. 3 Simple schematic of the geometry used for the FDTD scattering calculations for a single cell.



$$E_z^s(r', \omega) = -j\omega\hat{z}' \cdot A_z(r', \omega) + j\omega\eta\hat{r} \cdot F(r', \omega) \quad (25a)$$

$$A_z(r', \omega) = \frac{\mu}{4j} \int_{\Gamma} J_s(r', \omega) H_0^{(2)}[k|r-r'|] dl' \quad (25b)$$

$$F_z(r', \omega) = \frac{\epsilon}{4j} \int_{\Gamma} M_s(r', \omega) \cdot \hat{r} H_0^{(2)}[k|r-r'|] dl' \quad (25c)$$

Here,  $r$  is the point at far field. As  $|kr| \rightarrow \infty$ , the Hankel function can be written as:

$$H_0^{(2)}(kr) \sim \left(\frac{j2}{\pi kr}\right)^{1/2} e^{-jkr} \quad (25d)$$

The phase function describing a scattering pattern,  $F(\phi)$  is thus:

$$F(\phi) \sim \frac{ke^{j(\pi/4)}}{\sqrt{8\pi k}} \sum_{n=1}^N [-\eta\hat{z}' \cdot \vec{J}_{eq}(r') - \hat{z}' \times \vec{M}_{eq} \cdot \hat{r}] e^{jk\hat{r} \cdot r'} \Delta x \quad (25e)$$

Here  $\eta = \sqrt{\frac{\mu_0}{\epsilon_0}}$ ,  $k$  is the wave number,  $N$  is the number of segment on the virtual contour.  $\hat{z}'$  is the unit vector on  $z$  direction,  $\hat{r}$  is the unit vector of the far field point and  $\phi$  is the scattering angle.

## V. Validation of the FDTD Numerical Implementation

Validation for the numerical implementation of the above FDTD mathematical model was first carried out by comparing the predicted scattering patterns for homogeneous spheres based on the FDTD technique, against the results of Mie theory [37]. The grid size for the FDTD calculations was  $\lambda/40$ . The source pulse used in the simulations was a Gaussian pulse, propagating along the  $x$  direction defined as:

$$E_x^i(s, j) = \exp(-(t/\tau - 3)^2) \sin(2\pi f(t - 3\tau)) \quad (26)$$

In eqn. (26),  $E_x^i(s, j)$  is the line source,  $f$  is the central frequency of interest, and  $\tau$  is the characteristic time of the Gaussian pulse determined by the frequency bandwidth of interest.

Scattering fields were obtained at every grid point, as the Gaussian pulse propagated through the entire computation region. The number of time steps for the DFT computation [the  $n$  in eqn.(6)] was chosen to be sufficiently large to ensure the pulse magnitude approached zero. The phase function  $F(\phi)$  was computed after the FDTD was completed, in 5-degree increments. Results of the

scattering patterns obtained from FDTD simulations for scatterers with two different indexes of refraction ( $m=1.02$  and  $m=1.37$ ) are shown in Figs. 4a and 4b. Results of the Mie theory are also shown for comparison. The radius of the cell (assumed to be a homogeneous sphere placed in vacuum) was taken to be  $2\text{ }\mu\text{m}$ , while the chosen optical wavelength was also  $2\text{ }\mu\text{m}$ . The plots of Fig. 4 clearly show that the refraction index strongly affects the scattering pattern. The number of fluctuations increases with the refractive index. More importantly, results obtained from the FDTD technique match the predictions of Mie theory [37] fairly well. The agreement at small scattering angle ( $0\sim 50^\circ$ ) is particularly good, with a slight deviation at higher angles. This may be due to reflection at the boundaries and dispersion of scattered light within the FDTD grid. Fig. 5 shows that the comparison between FDTD and Mie theory for a  $0.535\text{ }\mu\text{m}$  circular object of dielectric constant 1.37, with extracellular fluid of relative permittivity 1.35 surrounding it. The cellular values were chosen in keeping with published data [38,39]. A  $0.6328\text{ }\mu\text{m}$  wavelength was used for these calculations, since it corresponds to that of a He-Ne laser, an optical source that is commonly used.

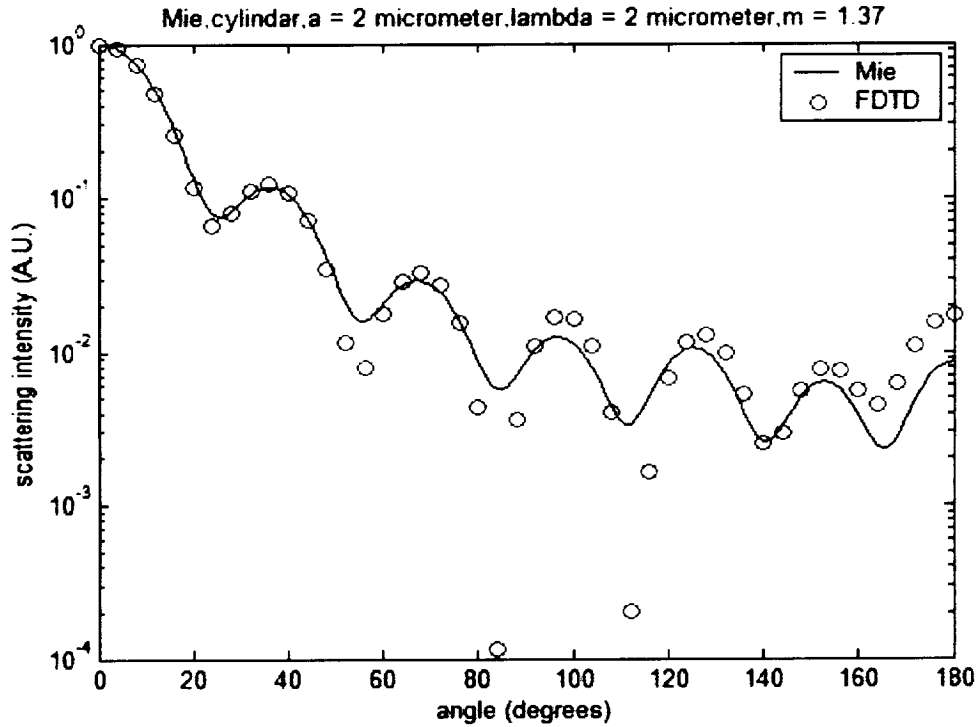


Fig. 4. Validation of the vacuum 2D TM FDTD code. The environment is vacuum. The index of refraction of cell is: (a)1.02, and (b)1.37.  $\lambda=2\text{ }\mu\text{m}$  and  $a=2\text{ }\mu\text{m}$ .

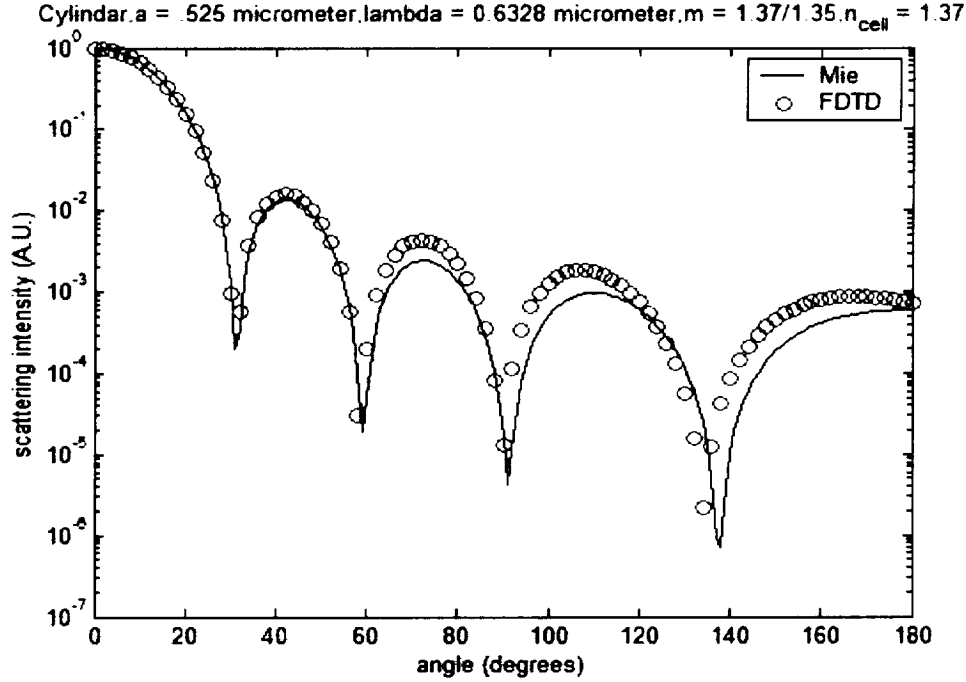


Fig.5. Validation of the 2D TM FDTD code. Index of refraction of cell is 1.37 and that of the environment fluid is 1.35. He-Ne laser wavelength ( $\lambda = 0.6328 \mu\text{m}$ ) is used.  $a = 0.525 \mu\text{m}$ .

These results once again reveal close agreement between the FDTD results and the Mie theory, thereby validating the electromagnetic model and its numerical implementation. Furthermore, Fig. 5 shows that the code is not only valid for simulations in vacuum, but also capable of treating spatially non-uniform relative permittivities.

## VI. The Alternating Direction Implicit (ADI) FDTD Method

Though the FDTD method is widely used for simulating electromagnetic problems, it has one significant drawback. It is based on the Courant-Friedrich-Levy (CFL) condition [29] that places a constraint on the time step for a given grid spacing. Under the traditional FDTD, smaller grid spacing (as would be required for complicated geometries with inflexion points, or sharp corners, or sizes comparable to the wavelengths) translates into a smaller time step. This increases the computational time and burden significantly. Also, analyses for high-frequency signals would be slow and time-consuming.

A method for overcoming this difficulty has recently been proposed [40] for two-dimensional problems that introduces an alternating direction implicit FDTD method (the ADI-FDTD approach). The method is based on the alternating direction implicit method of mathematics [41], and has been

applied to Yee's staggered cell [28] to solve Maxwell's equations. The ADI-FDTD scheme has recently been generalized to cover three-dimensional (3D) situations [42, 43].

Since the ADI-TDFD scheme is basically similar to the FDTD method already discussed, the details are not given here. However, the inherent equations that change due to the use of ADI, are presented and discussed below. The 3D space is discretized using the standard Yee-grid. Berenger's perfectly matched layer (PML) is used around the 3D computation region as the absorption boundary condition. It requires field splitting. Then the 6 conventional Maxwell equations are changed into 12. ADI demands the one FDTD time step into two steps. The equations used in the first  $1/2\Delta t$  are:

$$\epsilon \frac{E_{xy}|_{i+1/2,j,k}^{n+1/2} - E_{xy}|_{i+1/2,j,k}^n}{\Delta t/2} + \sigma_y E_{xy}|_{i+1/2,j,k}^n = \frac{H_{zx}|_{i+1/2,j+1/2,k}^{n+1/2} + H_{zy}|_{i+1/2,j+1/2,k}^{n+1/2} - (H_{zx}|_{i+1/2,j-1/2,k}^{n+1/2} + H_{zy}|_{i+1/2,j-1/2,k}^{n+1/2})}{\Delta y} \quad (27a)$$

$$\epsilon \frac{E_{xz}|_{i+1/2,j,k}^{n+1/2} - E_{xz}|_{i+1/2,j,k}^n}{\Delta t/2} + \sigma_z E_{xz}|_{i+1/2,j,k}^n = -\frac{H_{yx}|_{i+1/2,j,k+1/2}^n + H_{yz}|_{i+1/2,j,k+1/2}^n - (H_{yx}|_{i+1/2,j,k-1/2}^n + H_{yz}|_{i+1/2,j,k-1/2}^n)}{\Delta z} \quad (27b)$$

$$\epsilon \frac{E_{yz}|_{i,j+1/2,k}^{n+1/2} - E_{yz}|_{i,j+1/2,k}^n}{\Delta t/2} + \sigma_z E_{yz}|_{i,j+1/2,k}^n = \frac{H_{xy}|_{i,j+1/2,k+1/2}^{n+1/2} + H_{xz}|_{i,j+1/2,k+1/2}^{n+1/2} - (H_{xy}|_{i,j+1/2,k-1/2}^{n+1/2} + H_{xz}|_{i,j+1/2,k-1/2}^{n+1/2})}{\Delta z} \quad (27c)$$

$$\epsilon \frac{E_{yx}|_{i,j+1/2,k}^{n+1/2} - E_{yx}|_{i,j+1/2,k}^n}{\Delta t/2} + \sigma_x E_{yx}|_{i,j+1/2,k}^n = -\frac{H_{zx}|_{i+1/2,j+1/2,k}^n + H_{xz}|_{i+1/2,j+1/2,k}^n - (H_{yx}|_{i-1/2,j+1/2,k}^n + H_{xz}|_{i-1/2,j+1/2,k}^n)}{\Delta x} \quad (27d)$$

$$\epsilon \frac{E_{zx}|_{i,j,k+1/2}^{n+1/2} - E_{zx}|_{i,j,k+1/2}^n}{\Delta t/2} + \sigma_x E_{zx}|_{i,j,k+1/2}^n = \frac{H_{yx}|_{i+1/2,j,k+1/2}^{n+1/2} + H_{yz}|_{i+1/2,j,k+1/2}^{n+1/2} - (H_{yx}|_{i+1/2,j,k-1/2}^{n+1/2} + H_{yz}|_{i+1/2,j,k-1/2}^{n+1/2})}{\Delta x} \quad (27e)$$

$$\epsilon \frac{E_{zy}|_{i,j,k+1/2}^{n+1/2} - E_{zy}|_{i,j,k+1/2}^n}{\Delta t/2} + \sigma_y E_{zy}|_{i,j,k+1/2}^n = -\frac{H_{zx}|_{i,j+1/2,k+1/2}^n + H_{zy}|_{i,j+1/2,k+1/2}^n - (H_{zx}|_{i,j-1/2,k+1/2}^n + H_{zy}|_{i,j-1/2,k+1/2}^n)}{\Delta y} \quad (27f)$$

$$\mu \frac{H_{xy}|_{i,j+1/2,k+1/2}^{n+1/2} - H_{xy}|_{i,j+1/2,k+1/2}^n}{\Delta t/2} + \sigma_y^* H_{xy}|_{i,j+1/2,k+1/2}^n = -\frac{E_{zx}|_{i,j+1,k+1/2}^n + E_{zy}|_{i,j+1,k+1/2}^n - (E_{zx}|_{i,j,k+1/2}^n + E_{zy}|_{i,j,k+1/2}^n)}{\Delta y} \quad (27g)$$

$$\mu \frac{H_{xz}|_{i,j+1/2,k+1/2}^{n+1/2} - H_{xz}|_{i,j+1/2,k+1/2}^n}{\Delta t/2} + \sigma_z^* H_{xz}|_{i,j+1/2,k+1/2}^n = \frac{E_{yx}|_{i,j+1/2,k+1/2}^{n+1/2} + E_{yz}|_{i,j+1/2,k+1/2}^{n+1/2} - (E_{yx}|_{i,j+1/2,k-1/2}^{n+1/2} + E_{yz}|_{i,j+1/2,k-1/2}^{n+1/2})}{\Delta z} \quad (27h)$$

$$\mu \frac{H_{yz}|_{i+1/2,j,k+1/2}^{n+1/2} - H_{yz}|_{i+1/2,j,k+1/2}^n}{\Delta t/2} + \sigma_z^* H_{yz}|_{i+1/2,j,k+1/2}^n = -\frac{E_{xy}|_{i+1/2,j,k+1}^n + E_{xz}|_{i+1/2,j,k+1}^n - (E_{xy}|_{i+1/2,j,k}^n + E_{xz}|_{i+1/2,j,k}^n)}{\Delta z} \quad (27i)$$

$$\mu \frac{H_{yx}|_{i+1/2,j,k+1/2}^{n+1/2} - H_{yx}|_{i+1/2,j,k+1/2}^n}{\Delta t/2} + \sigma_x^* H_{yx}|_{i+1/2,j,k+1/2}^n = \frac{E_{zx}|_{i+1,j,k+1/2}^{n+1/2} + E_{zy}|_{i+1,j,k+1/2}^{n+1/2} - (E_{zx}|_{i,j,k+1/2}^{n+1/2} + E_{zy}|_{i,j,k+1/2}^{n+1/2})}{\Delta x} \quad (27j)$$

$$\mu \frac{H_{zx}|_{i+1/2,j+1/2,k}^{n+1/2} - H_{zx}|_{i+1/2,j+1/2,k}^n}{\Delta t/2} + \sigma_x^* H_{zx}|_{i+1/2,j+1/2,k}^n = -\frac{E_{yx}|_{i+1,j+1/2,k}^n + E_{yz}|_{i+1,j+1/2,k}^n - (E_{yx}|_{i,j+1/2,k}^n + E_{yz}|_{i,j+1/2,k}^n)}{\Delta x} \quad (27k)$$

$$\mu \frac{H_{zy}|_{i+1/2,j+1/2,k}^{n+1/2} - H_{zy}|_{i+1/2,j+1/2,k}^n}{\Delta t/2} + \sigma_y^* H_{zy}|_{i+1/2,j+1/2,k}^n = \frac{E_{xy}|_{i+1/2,j+1,k}^{n+1/2} + E_{xz}|_{i+1/2,j+1,k}^{n+1/2} - (E_{xz}|_{i+1/2,j,k}^{n+1/2} + E_{xy}|_{i+1/2,j,k}^{n+1/2})}{\Delta y} \quad (27m)$$

The equations used in the second  $1/2\Delta t$  are:

$$\varepsilon \frac{E_{xy}|_{i+1/2,j,k}^{n+1} - E_{xy}|_{i+1/2,j,k}^{n+1/2}}{\Delta t/2} + \sigma_y E_{xy}|_{i+1/2,j,k}^{n+1/2} = \frac{H_{xz}|_{i+1/2,j+1/2,k}^{n+1/2} + H_{zy}|_{i+1/2,j+1/2,k}^{n+1/2} - (H_{xz}|_{i+1/2,j-1/2,k}^{n+1/2} + H_{zy}|_{i+1/2,j-1/2,k}^{n+1/2})}{\Delta y} \quad (28a)$$

$$\varepsilon \frac{E_{xz}|_{i+1/2,j,k}^{n+1} - E_{xz}|_{i+1/2,j,k}^{n+1/2}}{\Delta t/2} + \sigma_z E_{xz}|_{i+1/2,j,k}^{n+1/2} = -\frac{H_{yx}|_{i+1/2,j,k+1/2}^{n+1} + H_{yz}|_{i+1/2,j,k+1/2}^{n+1} - (H_{yx}|_{i+1/2,j,k-1/2}^{n+1} + H_{yz}|_{i+1/2,j,k-1/2}^{n+1})}{\Delta z} \quad (28b)$$

$$\varepsilon \frac{E_{yz}|_{i,j+1/2,k}^{n+1} - E_{yz}|_{i,j+1/2,k}^{n+1/2}}{\Delta t/2} + \sigma_z E_{yz}|_{i,j+1/2,k}^{n+1/2} = \frac{H_{xy}|_{i,j+1/2,k+1/2}^{n+1/2} + H_{xz}|_{i,j+1/2,k+1/2}^{n+1/2} - (H_{xy}|_{i,j+1/2,k-1/2}^{n+1/2} + H_{xz}|_{i,j+1/2,k-1/2}^{n+1/2})}{\Delta z}$$

(28c)

$$\varepsilon \frac{E_{yx}|_{i,j+1/2,k}^{n+1} - E_{yx}|_{i,j+1/2,k}^{n+1/2}}{\Delta t/2} + \sigma_x E_{yx}|_{i,j+1/2,k}^{n+1/2} = - \frac{H_{zx}|_{i+1/2,j+1/2,k}^{n+1} + H_{zx}|_{i+1/2,j+1/2,k}^{n+1} - (H_{xy}|_{i-1/2,j+1/2,k}^{n+1} + H_{xz}|_{i-1/2,j+1/2,k}^{n+1})}{\Delta x}$$

(28d)

$$\varepsilon \frac{E_{xz}|_{i,j,k+1/2}^{n+1} - E_{xz}|_{i,j,k+1/2}^{n+1/2}}{\Delta t/2} + \sigma_x E_{xz}|_{i,j,k+1/2}^{n+1/2} = - \frac{H_{yx}|_{i+1/2,j,k+1/2}^{n+1/2} + H_{yz}|_{i,j+1/2,k+1/2}^{n+1/2} - (H_{yx}|_{i,j+1/2,k-1/2}^{n+1/2} + H_{yz}|_{i,j+1/2,k-1/2}^{n+1/2})}{\Delta x}$$

(28e)

$$\varepsilon \frac{E_{zy}|_{i,j,k+1/2}^{n+1} - E_{zy}|_{i,j,k+1/2}^{n+1/2}}{\Delta t/2} + \sigma_y E_{zy}|_{i,j,k+1/2}^{n+1/2} = - \frac{H_{xz}|_{i,j+1/2,k+1/2}^{n+1} + H_{zy}|_{i,j+1/2,k+1/2}^{n+1} - (H_{xz}|_{i,j-1/2,k+1/2}^{n+1} + H_{zy}|_{i,j-1/2,k+1/2}^{n+1})}{\Delta y}$$

(28f)

$$\mu \frac{H_{xy}|_{i,j+1/2,k+1/2}^{n+1} - H_{xy}|_{i,j+1/2,k+1/2}^{n+1/2}}{\Delta t/2} + \sigma_y^* H_{xy}|_{i,j+1/2,k+1/2}^{n+1/2} = - \frac{E_{xz}|_{i,j+1,k+1/2}^{n+1} + E_{zy}|_{i,j+1,k+1/2}^{n+1} - (E_{xz}|_{i,j,k+1/2}^{n+1} + E_{zy}|_{i,j,k+1/2}^{n+1})}{\Delta y}$$

(28g)

$$\mu \frac{H_{xz}|_{i,j+1/2,k+1/2}^{n+1} - H_{xz}|_{i,j+1/2,k+1/2}^{n+1/2}}{\Delta t/2} + \sigma_z^* H_{xz}|_{i,j+1/2,k+1/2}^{n+1/2} = - \frac{E_{yx}|_{i,j+1/2,k+1/2}^{n+1/2} + E_{yz}|_{i,j+1/2,k+1/2}^{n+1/2} - (E_{yx}|_{i,j+1/2,k-1/2}^{n+1/2} + E_{yz}|_{i,j+1/2,k-1/2}^{n+1/2})}{\Delta z}$$

(28h)

$$\mu \frac{H_{yz}|_{i+1/2,j,k+1/2}^{n+1} - H_{yz}|_{i+1/2,j,k+1/2}^{n+1/2}}{\Delta t/2} + \sigma_z^* H_{yz}|_{i+1/2,j,k+1/2}^{n+1/2} = - \frac{E_{xy}|_{i+1/2,j,k+1}^{n+1} + E_{xz}|_{i+1/2,j,k+1}^{n+1} - (E_{xy}|_{i+1/2,j,k}^{n+1} + E_{xz}|_{i+1/2,j,k}^{n+1})}{\Delta z}$$

(28i)

$$\mu \frac{H_{yx}|_{i+1/2,j,k+1/2}^{n+1} - H_{yx}|_{i+1/2,j,k+1/2}^{n+1/2}}{\Delta t/2} + \sigma_x^* H_{yx}|_{i+1/2,j,k+1/2}^{n+1/2} = - \frac{E_{xz}|_{i+1,j,k+1/2}^{n+1/2} + E_{zy}|_{i+1,j,k+1/2}^{n+1/2} - (E_{xz}|_{i,j,k+1/2}^{n+1/2} + E_{zy}|_{i,j,k+1/2}^{n+1/2})}{\Delta x}$$

(28j)

$$\mu \frac{H_{zx}|_{i+1/2,j+1/2,k}^{n+1} - H_{zx}|_{i+1/2,j+1/2,k}^{n+1/2}}{\Delta t/2} + \sigma_x^* H_{zx}|_{i+1/2,j+1/2,k}^{n+1/2} = - \frac{E_{yx}|_{i+1,j+1/2,k}^{n+1} + E_{yz}|_{i+1,j+1/2,k}^{n+1} - (E_{yx}|_{i,j+1/2,k}^{n+1} + E_{yz}|_{i,j+1/2,k}^{n+1})}{\Delta x}$$

(28k)

$$\mu \frac{H_{zy}|_{i+1/2,j+1/2,k}^{n+1} - H_{zy}|_{i+1/2,j+1/2,k}^{n+1/2}}{\Delta t/2} + \sigma_y^* H_{zy}|_{i+1/2,j+1/2,k}^{n+1/2} = - \frac{E_{xy}|_{i+1/2,j+1,k}^{n+1/2} + E_{xz}|_{i+1/2,j+1,k}^{n+1/2} - (E_{xy}|_{i+1/2,j,k}^{n+1/2} + E_{xz}|_{i+1/2,j,k}^{n+1/2})}{\Delta y}$$

(28m)

Bring (27k) and (27m) into (27a), we get:

$$\begin{aligned}
& -By|_{i+1/2,j,k} BBy|_{i+1/2,j-1,k} E_{xy}|_{i+1/2,j-1,k}^{n+1/2} + (1 + By|_{i+1/2,j,k} (BBy|_{i+1/2,j,k} + BBy|_{i+1/2,j-1,k})) E_{xy}|_{i+1/2,j,k}^{n+1/2} \\
& -By|_{i+1/2,j,k} BBy|_{i+1/2,j,k} E_{xy}|_{i+1/2,j+1,k}^{n+1/2} = Ay|_{i+1/2,j,k} E_{xy}|_{i+1/2,j,k}^n \\
& + By|_{i+1/2,j,k} (H_{zx}|_{i+1/2,j+1/2,k}^{n+1/2} - H_{zx}|_{i+1/2,j-1/2,k}^{n+1/2} + Kai|_{i+1/2,j+1/2,k} - Kai|_{i+1/2,j-1/2,k}) \\
& \text{Here } Kai|_{i+1/2,j+1/2,k} = AAy|_{i+1/2,j+1/2,k} H_{zy}|_{i+1/2,j+1/2,k}^n + BBy|_{i+1/2,j+1/2,k} (E_{xz}|_{i,j+1,k}^{n+1/2} - E_{xz}|_{i,j,k}^{n+1/2})
\end{aligned} \tag{27n}$$

(27n) is the implicit update expression of  $E_{xy}$ , a tri-diagonal matrix needs to be solved. In the same way, we can get the update expression of  $E_{yz}$  and  $E_{zx}$  in the first half step.

Bring (28i) and (28j) into (28a), we get:

$$\begin{aligned}
& -Bz|_{i+1/2,j,k} BBz|_{i+1/2,j,k-1} E_{xz}|_{i+1/2,j,k-1}^{n+1/2} + (1 + Bz|_{i+1/2,j,k} (BBz|_{i+1/2,j,k} + BBz|_{i+1/2,j,k-1})) E_{xz}|_{i+1/2,j,k}^{n+1/2} \\
& -Bz|_{i+1/2,j,k} BBz|_{i+1/2,j,k} E_{xz}|_{i+1/2,j,k+1}^{n+1/2} = Az|_{i+1/2,j,k} E_{xz}|_{i+1/2,j,k}^n \\
& + Bz|_{i+1/2,j,k} (H_{yx}|_{i+1/2,j,k+1/2}^{n+1/2} - H_{yx}|_{i+1/2,j,k-1/2}^{n+1/2} + Kai|_{i+1/2,j,k+1/2} - Kai|_{i+1/2,j,k-1/2})
\end{aligned} \tag{28n}$$

$$\text{Here } Kai|_{i+1/2,j,k+1/2} = AAz|_{i+1/2,j,k+1/2} H_{yz}|_{i+1/2,j,k+1/2}^n + BBz|_{i+1/2,j,k+1/2} (E_{xy}|_{i+1/2,j,k+1}^{n+1/2} - E_{xy}|_{i+1/2,j,k}^{n+1/2})$$

In the same way, we can get the update expression of  $E_{yx}$  and  $E_{zy}$  in the second half step.

The coefficient used in (27n) and (28n) are:

$$Aq|_{i,j,k} = \frac{1 - \frac{\sigma_{ijk} \Delta t}{4\epsilon_{ijk}}}{1 + \frac{\sigma_{ijk} \Delta t}{4\epsilon_{ijk}}}, q = x, y, z,$$

$$Bq|_{i,j,k} = \frac{\frac{\Delta t}{2\epsilon_{ijk}\Delta q}}{1 + \frac{\sigma_{ijk}^* \Delta t}{4\epsilon_{ijk}}}, q = x, y, z,$$

$$AAq|_{i,j,k} = \frac{1 - \frac{\sigma_{ijk}^* \Delta t}{4\mu_{ijk}}}{1 + \frac{\sigma_{ijk}^* \Delta t}{4\mu_{ijk}}}, q = x, y, z, \text{ and}$$

$$BBq|_{i,j,k} = \frac{\frac{\Delta t}{2\mu_{ijk}\Delta q}}{1 + \frac{\sigma_{ijk}^* \Delta t}{4\mu_{ijk}}}, q = x, y, z.$$

## VII. Simple Example Implementation and Results

Numerical codes were developed and implemented for electromagnetic calculations of the scattered fields and power, based on both the MM and hybrid schemes. The intent was to demonstrate that the simulation capability is successfully in place at Old Dominion University. These codes could be tested further for validation and refinement, and applied to real scattering problems with complex geometries. Here, the numerical codes were used only for a simple geometry and the calculation results presented in detail in the next section.

### VII.A MM – Related Calculations

A simple flat, two-dimensional (2D) rectangular geometry was considered lying in the  $z = 0$  plane. A frequency of 30 GHz was chosen. In accordance with the triangular patch basis functions for surfaces given in section III.A, this 2D plate was divided into 16 triangles with uniform grid spacings  $\Delta x = \Delta y (\equiv \Delta)$ , which was taken to be 1/10 of the operating wavelength. The extent along the x-axis was  $4\Delta$ , and  $2\Delta$  along the y-axis. In general, rectangular shapes with M and N segments along the x- and y-axes lead to  $2MN$  triangles, with a total number of basis functions  $N_{\text{basis}}$  (which requires an accounting of all mutually adjacent triangles) given by :  $N_{\text{basis}} = 3MN - M - N$ . Hence,



this geometry required 18 basis functions. All triangles had identical areas.

The numerical implementation has been carried out completely, with the corresponding source code written in FORTRAN. Results for the impedance matrix  $[Z]$  and the current were obtained, and are given below. The  $[Z]$  elements, which were complex, were as:

1 1 (3.4616823E-6,1.2840886E-3)	1 2 (3.2690945E-6,1.7910324E-5)
1 3 (3.0042051E-6,3.5189796E-6)	1 4 (2.624891E-6,8.7982584E-7)
1 5 (3.842653E-6,-4.7652775E-4)	1 6 (3.7359914E-6,2.0180203E-5)
1 7 (3.645482E-6,5.2011955E-6)	1 8 (6.8873705E-6,-3.243064E-5)
1 9 (6.489668E-6,3.6305928E-6)	1 10 (5.65048E-6,3.3914564E-6)
1 11 (4.454643E-6,3.6243454E-7)	1 12 (8.129872E-6,5.271748E-4)
1 13 (7.99366E-6,4.103712E-5)	1 14 (6.8798726E-6,7.3656983E-6)
1 15 (5.052641E-6,6.984539E-7)	1 16 (8.0954805E-7,-1.2388141E-5)
1 17 (5.4896554E-7,-3.2988587E-6)	1 18 (6.7900316E-7,-2.863137E-7)
2 1 (3.4260583E-6,2.027901E-5)	2 2 (3.4611057E-6,1.2538116E-3)
2 3 (3.4333897E-6,2.0456453E-5)	2 4 (3.295872E-6,4.305291E-6)
2 5 (3.994305E-6,-4.872825E-4)	2 6 (3.9615124E-6,-4.8804885E-4)
2 7 (4.065163E-6,2.2113232E-5)	2 8 (6.809017E-6,6.1009614E-6)
2 9 (7.0531405E-6,-2.9536808E-5)	2 10 (6.8078406E-6,5.577691E-6)
2 11 (6.072316E-6,4.264207E-6)	2 12 (7.40168E-6,3.0495348E-6)
2 13 (8.248924E-6,5.155328E-4)	2 14 (8.110917E-6,4.3091848E-5)
2 15 (6.9864927E-6,7.718715E-6)	2 16 (1.2968917E-6,2.6661093E-5)
2 17 (8.0898826E-7,-1.2277626E-5)	2 18 (7.586889E-7,-2.6439611E-6)
3 1 (3.0029814E-6,3.5050061E-6)	3 2 (3.2611687E-6,1.7748624E-5)
3 3 (3.4605432E-6,1.2235348E-3)	3 4 (3.5976945E-6,2.3002576E-5)
3 5 (3.7368145E-6,2.0052641E-5)	3 6 (3.875039E-6,-4.971584E-4)
3 7 (4.0803574E-6,-4.995696E-4)	3 8 (5.936471E-6,4.206562E-6)
3 9 (6.8089975E-6,6.1009304E-6)	3 10 (7.2189095E-6,-2.6642956E-5)
3 11 (7.126019E-6,7.5248003E-6)	3 12 (5.821322E-6,1.0841968E-6)
3 13 (7.5135926E-6,3.8112284E-6)	3 14 (8.367975E-6,5.038911E-4)
3 15 (8.228179E-6,4.514658E-5)	3 16 (1.6828574E-6,1.5951882E-5)
3 17 (1.068182E-6,2.3982657E-5)	3 18 (8.084246E-7,-1.2167126E-5)
4 1 (2.2702647E-6,5.3112523E-7)	4 2 (2.7109927E-6,2.7208943E-6)
4 3 (3.0962701E-6,1.5218275E-5)	4 4 (3.4599738E-6,1.193258E-3)
4 5 (3.179949E-6,4.42893E-6)	4 6 (3.4069671E-6,1.812755E-5)
4 7 (3.7557738E-6,-5.070338E-4)	4 8 (4.4610433E-6,4.2454996E-7)
4 9 (5.7958486E-6,3.9000697E-6)	4 10 (6.8089884E-6,6.1009163E-6)
4 11 (7.384672E-6,-2.3749117E-5)	4 12 (3.7453246E-6,-1.5543089E-6)
4 13 (5.9176313E-6,1.258488E-6)	4 14 (7.6254937E-6,4.572916E-6)
4 15 (8.487027E-6,4.922489E-4)	4 16 (1.8918652E-6,4.909446E-6)
4 17 (1.2615717E-6,1.427646E-5)	4 18 (8.3947156E-7,2.1304206E-5)
5 1 (1.3282961E-6,-5.065996E-4)	5 2 (1.2004091E-6,-5.121067E-4)
5 3 (1.5254552E-6,1.7916516E-5)	5 4 (2.1189257E-6,5.4923284E-6)
5 5 (-3.390591E-6,5.512347E-4)	5 6 (-2.9263424E-6,2.1411299E-5)
5 7 (-1.4370028E-6,7.5093394E-6)	5 8 (-1.8144461E-6,-1.8135617E-5)
5 9 (-1.4428904E-6,2.5558926E-5)	5 10 (-3.9065594E-7,1.3647906E-5)
5 11 (1.0101412E-6,6.0330712E-6)	5 12 (-3.9784663E-7,-4.2573123E-5)
5 13 (-1.857216E-7,-3.6293978E-4)	5 14 (-2.5795543E-9,6.418809E-6)

5 15 (1.2666419E-7,8.195884E-7)	5 16 (-1.2482839E-6,-3.116474E-5)
5 17 (-9.1828565E-7,1.8520703E-6)	5 18 (2.233487E-7,5.4667475E-6)
6 1 (1.5312934E-6,1.7810573E-5)	6 2 (1.2081355E-6,-5.2171933E-4)
6 3 (1.3194917E-6,-5.397907E-4)	6 4 (1.8564879E-6,2.0057238E-5)
6 5 (-2.9398602E-6,2.1336144E-5)	6 6 (-3.3916628E-6,5.2096135E-4)
6 7 (-2.6039947E-6,2.6274956E-5)	6 8 (-1.5219584E-6,-4.0074432E-6)
6 9 (-1.6989104E-6,-1.696899E-5)	6 10 (-1.0989961E-6,2.9860565E-5)
6 11 (1.3675981E-7,1.5700189E-5)	6 12 (-4.518921E-7,-5.8954824E-6)
6 13 (-2.3212505E-7,-3.8739046E-5)	6 14 (-1.7742081E-8,-3.8043613E-4)
6 15 (1.5408455E-7,7.4791037E-6)	6 16 (-1.0718904E-6,-5.079302E-7)
6 17 (-1.4137604E-6,-3.378447E-5)	6 18 (-7.662204E-7,2.6550505E-6)
7 1 (1.6527874E-6,4.688458E-6)	7 2 (1.1994189E-6,1.5679585E-5)
7 3 (1.0879746E-6,-5.368387E-4)	7 4 (1.4385755E-6,-5.6747434E-4)
7 5 (-2.0019865E-6,5.8753985E-6)	7 6 (-3.2622435E-6,1.6494674E-5)
7 7 (-3.392731E-6,4.9068755E-4)	7 8 (-9.989093E-7,-6.683132E-8)
7 9 (-1.6255885E-6,-4.283884E-6)	7 10 (-1.5833828E-6,-1.5802372E-5)
7 11 (-7.550989E-7,3.4162192E-5)	7 12 (-4.809328E-7,-1.7230377E-6)
7 13 (-3.0034254E-7,-5.2971372E-6)	7 14 (-6.639891E-8,-3.490495E-5)
7 15 (1.5023443E-7,-3.9793216E-4)	7 16 (-5.961662E-7,4.2460965E-6)
7 17 (-1.5414896E-6,-3.4250051E-6)	7 18 (-1.5792373E-6,-3.640419E-5)
8 1 (-2.4519601E-7,-4.0247177E-5)	8 2 (-1.8736351E-8,-8.539237E-8)
8 3 (5.7997033E-7,3.2883967E-6)	8 4 (1.2973869E-6,2.293018E-6)
8 5 (-4.2161655E-6,-1.7798244E-5)	8 6 (-3.608613E-6,-4.5680812E-6)
8 7 (-2.171954E-6,5.6421765E-7)	8 8 (-4.3539766E-6,1.2117194E-3)
8 9 (-3.8866637E-6,9.593817E-6)	8 10 (-2.6280004E-6,2.2516192E-6)
8 11 (-9.785879E-7,2.4496607E-6)	8 12 (-2.8783417E-6,-4.961151E-4)
8 13 (-2.95137E-6,-3.568135E-5)	8 14 (-2.7093383E-6,-6.0720803E-6)
8 15 (-2.1892651E-6,-1.5354407E-6)	8 16 (-1.3838471E-6,-5.068088E-4)
8 17 (-6.315448E-7,1.8196948E-5)	8 18 (6.16491E-7,5.833969E-6)
9 1 (-1.4798275E-8,1.2888796E-7)	9 2 (-8.154793E-8,-3.7371471E-5)
9 3 (2.9762952E-7,1.8544936E-6)	9 4 (1.000247E-6,4.158571E-6)
9 5 (-3.9725105E-6,1.6900563E-5)	9 6 (-4.215389E-6,-1.7674862E-5)
9 7 (-3.3975948E-6,-3.9080623E-6)	9 8 (-4.04241E-6,6.700779E-6)
9 9 (-4.3537E-6,1.1814693E-3)	9 10 (-3.721967E-6,1.2143675E-5)
9 11 (-2.3361235E-6,3.0384974E-6)	9 12 (-2.5874437E-6,1.2639825E-6)
9 13 (-2.997729E-6,-5.058632E-4)	9 14 (-3.0687801E-6,-3.7736066E-5)
9 15 (-2.8159452E-6,-6.4250875E-6)	9 16 (-1.5348432E-6,-5.162637E-4)
9 17 (-1.2655715E-6,-5.1834876E-4)	9 18 (-3.0247724E-7,2.0127358E-5)
10 1 (3.0580008E-7,2.8626718E-6)	10 2 (-1.6605337E-8,1.1569311E-7)
10 3 (8.21002E-8,-3.449577E-5)	10 4 (6.139951E-7,3.7944073E-6)
10 5 (-3.123678E-6,1.1625751E-5)	10 6 (-4.1998005E-6,1.4231362E-5)
10 7 (-4.214612E-6,-1.7551507E-5)	10 8 (-3.2069831E-6,6.613143E-7)
10 9 (-4.206985E-6,4.17734E-6)	10 10 (-4.353419E-6,1.1512191E-3)
10 11 (-3.5572693E-6,1.4693527E-5)	10 12 (-2.0479958E-6,-5.5485156E-7)
10 13 (-2.699236E-6,5.02313E-7)	10 14 (-3.1171157E-6,-5.1561126E-4)
10 15 (-3.186187E-6,-3.9790753E-5)	10 16 (-1.2910064E-6,1.4239511E-5)
10 17 (-1.6546347E-6,-5.261443E-4)	10 18 (-1.1472957E-6,-5.298888E-4)
11 1 (6.2651E-7,1.7669165E-6)	11 2 (1.6354984E-7,2.5524761E-6)
11 3 (-1.8407604E-8,1.0251813E-7)	11 4 (2.4574524E-7,-3.1620053E-5)
11 5 (-1.8757693E-6,4.3743116E-6)	11 6 (-3.5438156E-6,9.9529424E-6)
11 7 (-4.4270946E-6,1.156214E-5)	11 8 (-2.0360366E-6,1.4151904E-6)
11 9 (-3.498722E-6,-1.2194391E-7)	11 10 (-4.3715613E-6,1.6539116E-6)

11 11 (-4.353149E-6,1.1209687E-3)	11 12 (-1.3598656E-6,3.383081E-7)
11 13 (-2.1443024E-6,-7.2913536E-7)	11 14 (-2.8110275E-6,-2.593456E-7)
11 15 (-3.2365041E-6,-5.2535894E-4)	11 16 (-7.775048E-7,3.5555772E-6)
11 17 (-1.6209246E-6,1.2313833E-5)	11 18 (-1.7744276E-6,-5.3602457E-4)
12 1 (4.86008E-6,5.2826735E-4)	12 2 (4.4065127E-6,8.269442E-7)
12 3 (3.4827353E-6,1.0371624E-6)	12 4 (2.2930721E-6,-6.2110854E-7)
12 5 (4.0270933E-6,-3.307024E-5)	12 6 (3.3456917E-6,-4.278911E-6)
12 7 (2.268097E-6,-2.0473858E-6)	12 8 (5.769255E-6,-4.6229013E-4)
12 9 (5.07908E-6,5.9779922E-6)	12 10 (3.7358036E-6,-7.795356E-7)
12 11 (2.0555075E-6,-2.1821397E-6)	12 12 (4.6326836E-6,6.4045283E-4)
12 13 (4.359218E-6,-1.3717479E-5)	12 14 (3.4564918E-6,-2.4191292E-6)
12 15 (2.1456116E-6,-2.2294877E-6)	12 16 (3.1911517E-6,4.1785286E-5)
12 17 (2.5026731E-6,6.014091E-6)	12 18 (1.6217407E-6,7.148078E-7)
13 1 (4.7143912E-6,3.7682817E-5)	13 2 (4.8215156E-6,5.119455E-4)
13 3 (4.371323E-6,9.165892E-7)	13 4 (3.4536001E-6,1.0199728E-6)
13 5 (4.211872E-6,-3.24895E-4)	13 6 (4.0555864E-6,-3.173011E-5)
13 7 (3.3735E-6,-4.061778E-6)	13 8 (5.6774297E-6,-2.0338608E-5)
13 9 (5.808194E-6,-4.4598E-4)	13 10 (5.1145066E-6,5.8891073E-6)
13 11 (3.7652316E-6,-7.6195806E-7)	13 12 (4.267819E-6,-1.1276143E-5)
13 13 (4.6897002E-6,6.35869E-4)	13 14 (4.414308E-6,-1.3024182E-5)
13 15 (3.505615E-6,-2.2868644E-6)	13 16 (3.5342582E-6,3.636501E-4)
13 17 (3.1629147E-6,4.0453294E-5)	13 18 (2.4745818E-6,5.796431E-6)
14 1 (4.045937E-6,6.0831753E-6)	14 2 (4.675405E-6,3.6672034E-5)
14 3 (4.7829576E-6,4.95624E-4)	14 4 (4.3361346E-6,1.0062317E-6)
14 5 (3.7910394E-6,8.388228E-6)	14 6 (4.237981E-6,-3.2915631E-4)
14 7 (4.084074E-6,-3.038997E-5)	14 8 (4.7860794E-6,-1.8788076E-6)
14 9 (5.7168763E-6,-1.932701E-5)	14 10 (5.8471296E-6,-4.2966983E-4)
14 11 (5.1499346E-6,5.8002206E-6)	14 12 (3.3006272E-6,-2.1873131E-6)
14 13 (4.3222653E-6,-1.068665E-5)	14 14 (4.7467165E-6,6.3128536E-4)
14 15 (4.469397E-6,-1.23309E-5)	14 16 (3.442733E-6,1.0234307E-6)
14 17 (3.507475E-6,3.679107E-4)	14 18 (3.1346801E-6,3.9121303E-5)
15 1 (2.9906414E-6,1.0069923E-6)	15 2 (4.0093536E-6,5.9297226E-6)
15 3 (4.6364134E-6,3.566128E-5)	15 4 (4.7443963E-6,4.7930201E-4)
15 5 (2.8951822E-6,6.0595147E-7)	15 6 (3.8135476E-6,8.257315E-6)
15 7 (4.2640926E-6,-3.3341735E-4)	15 8 (3.3111055E-6,-2.0225952E-6)
15 9 (4.823016E-6,-1.7244968E-6)	15 10 (5.756332E-6,-1.8315402E-5)
15 11 (5.886068E-6,-4.133595E-4)	15 12 (1.9609688E-6,-2.219029E-6)
15 13 (3.3484016E-6,-2.0766692E-6)	15 14 (4.3767076E-6,-1.00971665E-5)
15 15 (4.803733E-6,6.267012E-4)	15 16 (2.9495506E-6,1.1702908E-6)
15 17 (3.4199235E-6,1.1537359E-6)	15 18 (3.4806917E-6,3.7217108E-4)
16 1 (3.1832396E-6,-1.2917593E-5)	16 2 (3.43567E-6,3.0039517E-5)
16 3 (3.746049E-6,1.5019422E-5)	16 4 (3.9389565E-6,5.3375906E-6)
16 5 (2.4329631E-6,-2.4869798E-5)	16 6 (2.3665334E-6,4.399628E-6)
16 7 (2.7302235E-6,5.62648E-6)	16 8 (6.785991E-6,-4.7987667E-4)
16 9 (6.5537283E-6,-4.780589E-4)	16 10 (6.0897586E-6,2.0778683E-5)
16 11 (5.401115E-6,5.2356112E-6)	16 12 (7.867391E-6,5.731445E-5)
16 13 (7.816293E-6,3.2658965E-4)	16 14 (6.8187973E-6,6.3021616E-8)
16 15 (5.09427E-6,-1.9881284E-7)	16 16 (4.5478827E-7,5.852904E-4)
16 17 (4.943645E-7,2.4520778E-5)	16 18 (1.1977281E-6,7.844572E-6)
17 1 (2.9264238E-6,-1.7075954E-6)	17 2 (3.2961843E-6,-1.1774497E-5)
17 3 (3.7765526E-6,3.432097E-5)	17 4 (4.271087E-6,1.7065055E-5)
17 5 (2.52383E-6,3.9494016E-6)	17 6 (2.2696715E-6,-2.7472983E-5)

17 7 (2.5204165E-6,5.2169916E-6)	17 8 (6.4145865E-6,2.2780714E-5)
17 9 (6.6664656E-6,-4.949858E-4)	17 10 (6.6735424E-6,-5.057028E-4)
17 11 (6.4213836E-6,2.2922446E-5)	17 12 (6.799824E-6,9.558169E-6)
17 13 (7.701049E-6,5.3480434E-5)	17 14 (7.648538E-6,3.1383574E-4)
17 15 (6.6619795E-6,-9.972264E-7)	17 16 (8.3751774E-7,2.9638471E-5)
17 17 (4.5446495E-7,5.5500923E-4)	17 18 (8.155057E-7,2.9356284E-5)
18 1 (2.3686616E-6,-2.2426502E-7)	18 2 (2.820383E-6,-1.993386E-6)
18 3 (3.4091262E-6,-1.0631396E-5)	18 4 (4.117441E-6,3.8602403E-5)
18 5 (2.4565272E-6,5.6154176E-6)	18 6 (2.055875E-6,1.0388953E-6)
18 7 (2.1063815E-6,-3.007615E-5)	18 8 (5.3973044E-6,5.2112973E-6)
18 9 (6.0832644E-6,2.0650237E-5)	18 10 (6.546939E-6,-5.1009486E-4)
18 11 (6.7933647E-6,-5.3334643E-4)	18 12 (5.0371545E-6,1.2531445E-6)
18 13 (6.64835E-6,8.959851E-6)	18 14 (7.5347065E-6,4.9646412E-5)
18 15 (7.4807785E-6,3.0108174E-4)	18 16 (1.2029079E-6,7.8511675E-6)
18 17 (5.139923E-7,2.4796653E-5)	18 18 (4.5413707E-7,5.2472803E-4).

The current magnitudes were as:

1 (-7.0488726E-4,-4.1359872E-3)	2 (-3.259895E-4,3.7869822E-4)
3 (1.1044028E-3,9.498428E-3)	4 (1.0851541E-3,7.1884454E-3)
5 (-1.6145814E-3,-7.883782E-3)	6 (4.3422586E-4,7.928428E-3)
7 (1.9769833E-3,0.015651448)	8 (-6.5302517E-4,-2.8714612E-3)
9 (-9.280766E-4,-2.6803847E-3)	10 (8.852718E-4,9.267416E-3)
11 (6.842111E-4,5.6747663E-3)	12 (-1.2921324E-5,1.349302E-3)
13 (-6.516619E-4,-2.5269184E-3)	14 (-3.2737554E-4,5.139351E-4)
15 (-9.80073E-4,-3.3341408E-3)	16 (-1.3548372E-3,-6.1254217E-3)
17 (-1.5530751E-4,3.6133027E-3)	18 (2.0707286E-3,0.016081538).

Code for the hybrid MoM-PO technique was similarly developed. However, the hybrid MoM-PO scheme simplifies for a planar geometry for the following reason. In the hybrid scheme, the full, self-consistent solution is to be obtained through an iterative procedure. First, the currents in the PO region can be taken to be zero (an initial guess), while the usual MoM solution applied to the MoM zone. This yields the current distributions  $\mathbf{J}_1$  over the MoM region by solving :  $\mathbf{L}_e[\mathbf{J}_1(\mathbf{r})] + \mathbf{L}_e[\mathbf{J}_2(\mathbf{r})] = -\mathbf{E}^{\text{inc}}_{\text{tan}}(\mathbf{r})$  , for  $\mathbf{r} \in \text{MMZ}$  , and  $\mathbf{J}_2(\mathbf{r}) = 0$ . Next, this value of  $\mathbf{J}_1$  is used to update the current distribution in the PO region according to:  $\mathbf{J}_2(\mathbf{r}) = 2 \mathbf{n}^\wedge \times \mathbf{H}^{\text{inc}}(\mathbf{r}) + \mathbf{L}_h[\mathbf{J}_1(\mathbf{r})] + \mathbf{L}_h[\mathbf{J}_2(\mathbf{r})]$  , for  $\mathbf{r} \in \text{POSR}$  , where  $\mathbf{n}^\wedge$  is the unit surface normal, and the operators  $\mathbf{L}_e[\mathbf{J}(\mathbf{r})]$  and  $\mathbf{L}_h[\mathbf{J}(\mathbf{r})]$  defined previously in eqn. (14). For planar structure, both  $\mathbf{J}(\mathbf{r}')$  and  $\nabla' G(\mathbf{r},\mathbf{r}')$  are in the plane. Hence,  $\mathbf{J}(\mathbf{r}') \times [\nabla' G(\mathbf{r},\mathbf{r}')]$  is perpendicular to the plane. Due to the “cross-product” with the normal vector, a zero value results for  $\mathbf{L}_h[\mathbf{J}(\mathbf{r})] = 2 \mathbf{n}^\wedge \times \int \int_S \mathbf{J}(\mathbf{r}') \times [\nabla' G(\mathbf{r},\mathbf{r}')] dS'$  . Hence, only the

$2 \mathbf{n}^\wedge \times \mathbf{H}^{inc}(\mathbf{r})$  term appears in the PO region. Our simulations for simple 2D geometries did yield this result, and hence, the hybrid scheme simplified, and did not require the use of an iterative technique for convergence. The detailed numerical values are, therefore, not included in this report.

### VIII. Results for the Two-Dimensional FDTD Scheme

The two-dimensional FDTD code developed was applied for time-dependent simulations of scattering from biological cells. Since these cells function as dielectrics with finite conductivity, the application becomes more general than the “perfect-conductor” scenarios. There is also some interest in electromagnetic interactions with biological cells. Hence, some examples of light-scattering off biological cells using the 2D FDTD code were used & are presented here.

As is well known, Mie theory has the two following fundamental limitations. (i) The incident energy has to be in the form of a plane wave. This has recently been circumvented by the development of a generalized Lorenz-Mie theory [44] that allows for the interaction between spheres and arbitrary incident beams. (ii) A spherical geometry and homogeneity of the scatter. While recent techniques have been developed to treat multi-layered spheres [45,46], the angular symmetry remains a constraint. The FDTD approach used here circumvents such restrictions, and allows for the inclusion of a heterogeneous structure, arbitrary shapes, and complex, non-concentric dielectric distributions. Having validated the FDTD method with Mie theory for the simple, homogeneous,

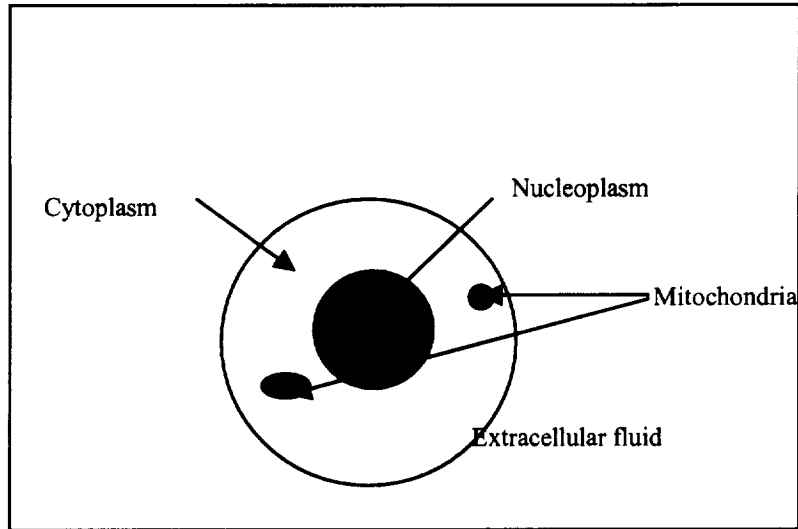


Fig. 6. Simple representation of cell parts with different index of refraction.

spherical case, results of the scattering patterns are now presented for the more realistic and complex cellular shapes.

Different parts of a biological cell have different index of refraction as shown schematically in Fig. 6. Hence, cellular scattering patterns can potentially reveal various geometries of sub-cellular structures, their relative size and physical location relative to the center. For example, the angular scattering patterns can be obtained by changing the orientation of the incident optical light. If these were to be compared to the theoretical predictions for various shapes and sizes on the internal sub-structure, then the geometry, and size could be inferred. Similarly, changes in morphology (for example between healthy and malignant cells, or upon electromagnetic pulse exposure) can similarly be obtained. Some experimental work, in this regard, already exists. For example, Mourant et al. [47] showed that organelles smaller in size than the nucleus were responsible for significant scattering contributions. Measurements also indicate that the nucleus is responsible for low-angle scattering, while smaller organelles produced high-angle scattering.

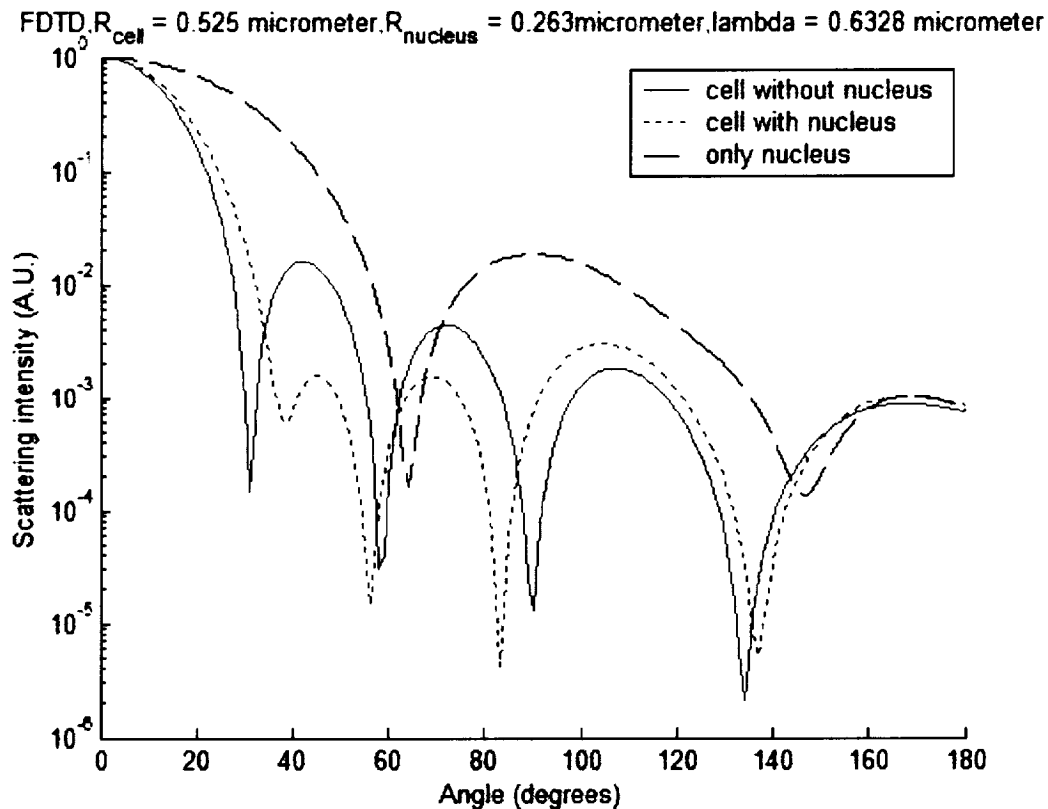


Fig.7. Cellular scattering patterns of cell with nucleus and without nucleus.

Fig. 7 shows FDTD results of the cellular scattering patterns for cell with nucleus and without a nucleus for an incident wavelength of  $0.6328 \mu\text{m}$ , which correspond to a He-Ne laser source. In keeping with published reports [39], the refractive index of the nucleus and cellular cytoplasm were set to 1.39 and 1.37, respectively. The extra-cellular fluid was taken to be 1.35 [38]. The cell radius was  $0.525 \mu\text{m}$ , while the nuclear radius was  $0.263 \mu\text{m}$ . The patterns show that the nucleus brings about much more change at low angles than at higher angles. This is because the existence of a nucleus changes the forward scattering more significantly than backscattering. This prediction is in keeping with the experimental observations of Mourant et al. [47]. Cells with mitochondria were also simulated. The scattering patterns obtained, for cells of radius  $0.525 \mu\text{m}$  are shown in Fig. 8. Both of the two cells had identical nuclei. As apparent from the curves of Fig. 8, the existence of mitochondria is predicted to lead to stronger backscattered intensity. Also, the scattering pattern is seen to change only at the higher angles. This trend also agrees well with measured data [47] suggesting the organelles can significantly change the higher-angle patterns. Thus, any morphological changes or electromagnetic field impact on the organelles (as in intra-cellular electroporation), is likely to be diagnosed through such optical scattering.

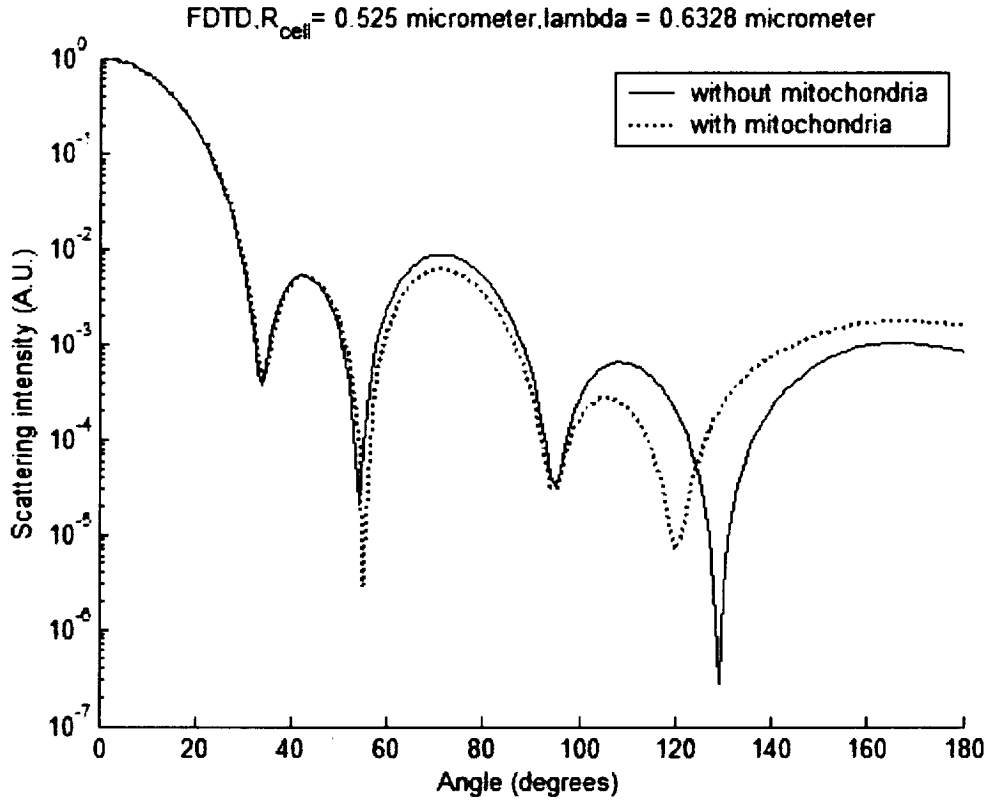


Fig. 8. Scattering patterns of cell with nucleus, with and without mitochondria.

All models used in literature implicitly assume that the nucleus is located at the center of a cell, and that its shape is spherical [48,49]. However, this is a simplification, and in reality, the nucleus can have a number of different shapes and can be located anywhere inside a biological cell. The size, position and shape can all have an effect on the scattering patterns as demonstrated through the FDTD simulations. The results shown in Fig. 9 reveal the scattering patterns of cells with different nuclear sizes for a fixed outer cell size. The outer cell radius was again set at  $0.525 \mu\text{m}$ , while the Ne-He laser characteristic wavelength of  $0.6328 \mu\text{m}$  was used. With increasing size of the nucleus, the scattering intensity is predicted to increase as may be expected. Furthermore, the change in the scattering pattern is most pronounced at larger-angles. Hence, the backscattering configuration would be most sensitive for detecting such information. It is also apparent that as the size of the nucleus gets progressively smaller, there would not be much change in the scattering pattern and so the sensitivity would reduce. Hence, a size threshold is probably inherent from practical detector considerations. Furthermore, if sizes of the nucleus were the same, but a nucleus was located at different positions inside the cell, then again differences in the scattering pattern are predicted. This

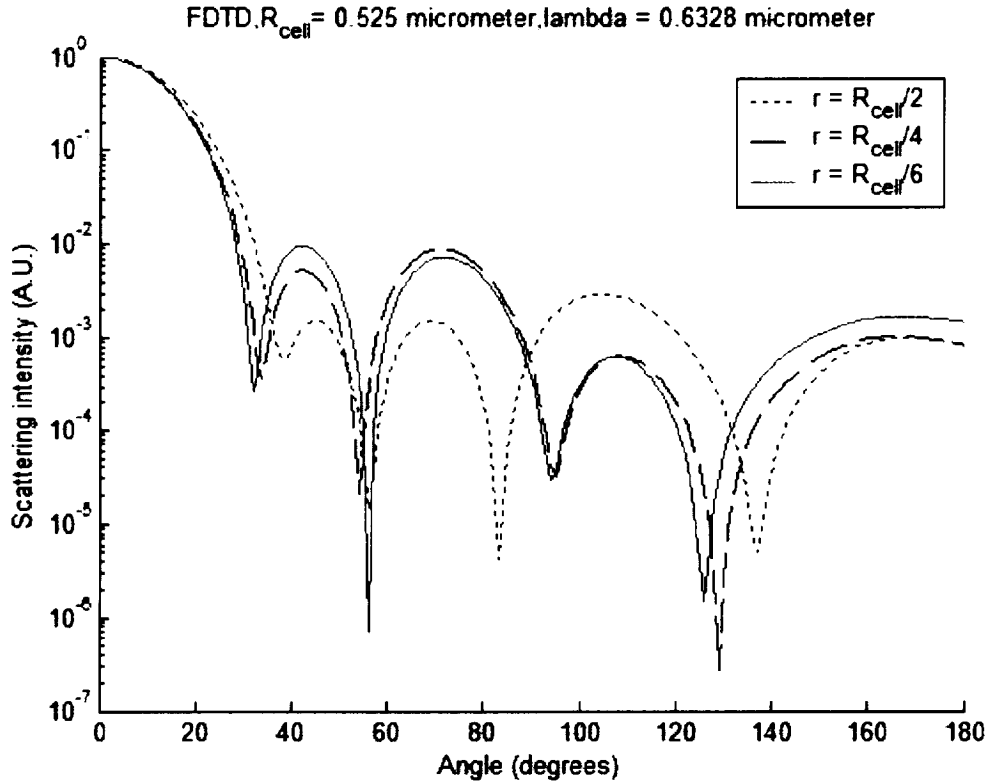


Fig. 9. Cellular scattering patterns of cells with different sizes of nucleus.



is shown through the results of Fig. 10. Two situations have been considered: one in which nuclei are positioned at the same radial distance from the center of the cell. However, their angular orientation relative to the incoming wave is different. A second situation is that of an identical nucleus positioned at the cell center. As seen from the results of Fig. 10, the scattering patterns for the former situation do not change significantly, and are all close to each other. However, they are all quite different from that for the center-located nuclear cell, and also have slightly higher intensities. The absence of sharp minima in the scattering pattern could, for example, be indicative of nuclei that were off-center in biological cells. Another case considered here is that of a nucleus located at different distances from the center of the cell. The results are shown in Fig. 11 with the relative orientation with respect to the incident wave being fixed. The scattering patterns once again reveals that changes are most likely to occur at higher angles (i.e., backscattering geometry). It is also apparent that the scattering pattern is affected by the relative distance of the nucleus from the center, but not, the absolute location.

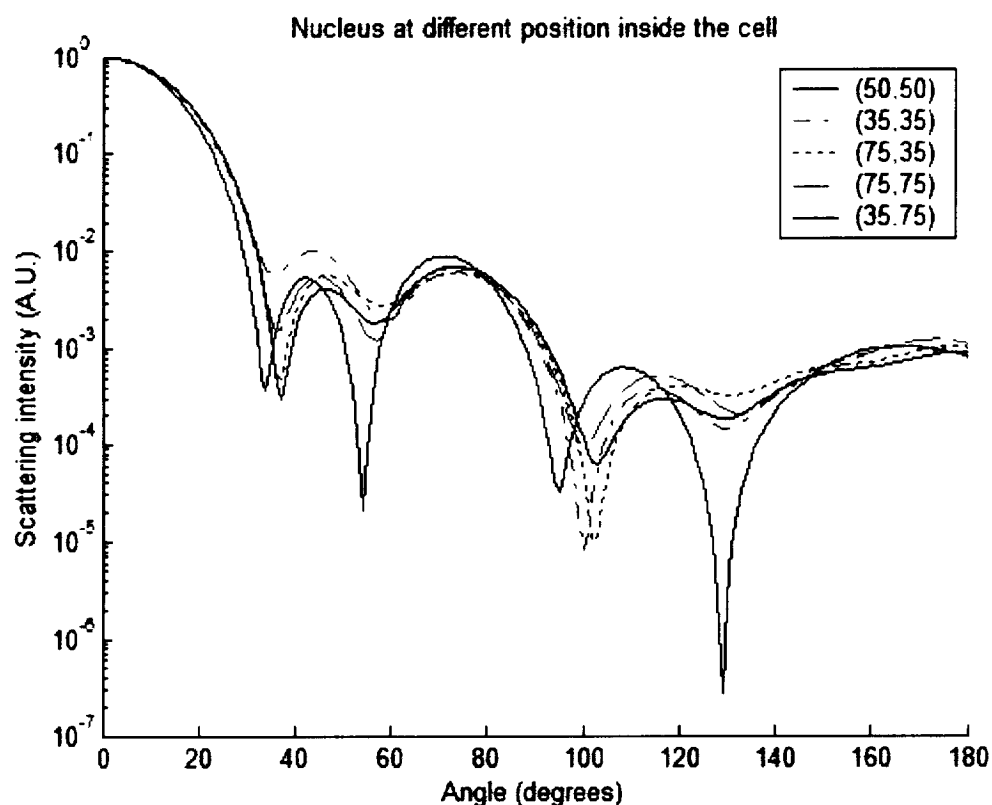


Fig. 10. Scattering patterns of cells with nucleus at the same distance from the centers of the cells.

## IX. Results for the Three-Dimensional ADI-FDTD Scheme

A three-dimensional (3D) ADI-FDTD simulation scheme was developed and implemented. The primary advantages of such an ADI-TDFD technique can be summarized as follows:

- (i) It allows for both a complete time-domain analysis and the steady-state result. The latter can result by running the simulations up to longer times. The transient behavior cannot be obtained from the Moment Method or PO-MoM schemes.
- (ii) The ADI-FDTD allows for any arbitrary geometry including sharp corners and complex features.
- (iii) It is significantly faster than the FDTD scheme since very large time steps can be used without the need to be restricted to the CFL condition.
- (iv) High frequency analysis for which the spatial discretization has to be small, can be carried

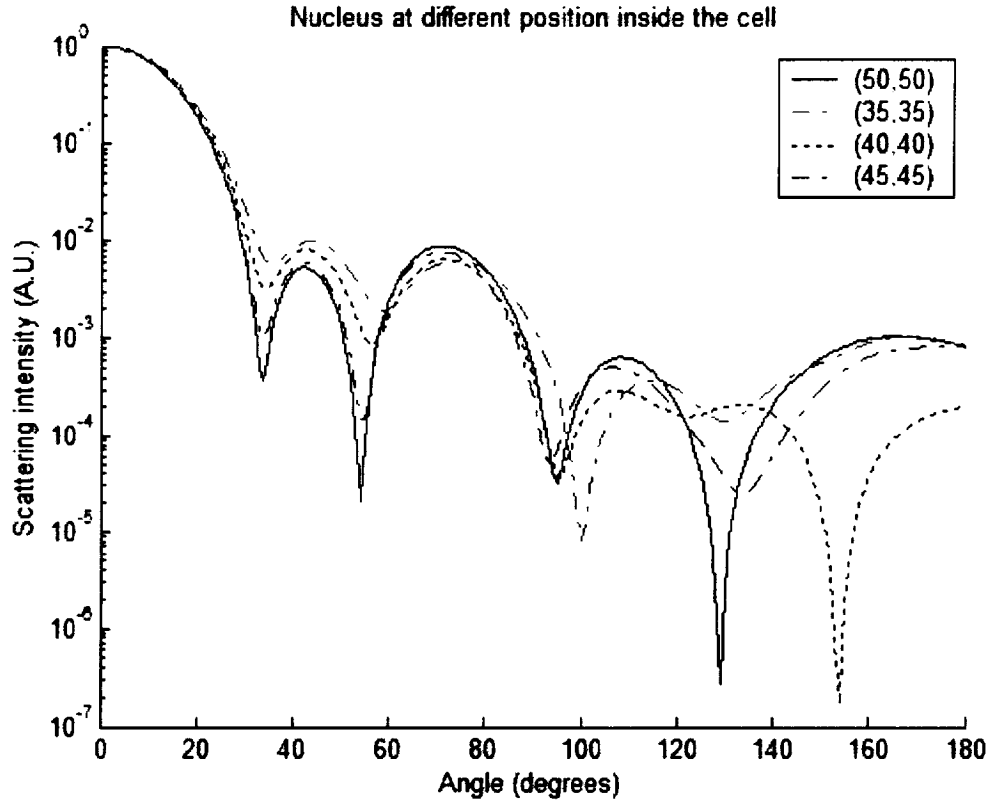


Fig. 11. Scattering patterns of cells with nucleus at different distances from the centers of cells.

out relatively easily as the time-step can remain large. Similarly, the technique is of advantage for large objects for which many grid points may be required.

- (v) Non-uniform, multi-grids can be employed for better resolution. Also, absorbing boundary conditions can be implemented for accurate analyses.
- (vi) Finally, dielectrics or perfect conductors or both can be studied with ADI-FDTD.

The first set of results that are given below, emphasize the significant increase in time step that can be achieved through the ADI-FDTD scheme as compared to the traditional FDTD method. A simple electric field pulse was taken for simplicity. The traditional FDTD required a time step of about  $2.476 \times 10^{-17}$  s. Fig. 12a shows the electric field waveform of an assumed source (single pulse), and also the time-dependent E-field at an observation point slightly “downstream”. The time step was chosen to equal the normal CFL (CFLN) value, and hence, was very small. Fig. 12(b) shows the numerical results of the E-field as a function of time, but with a time step chosen to be 1000 times larger. The source E-field pulse was correspondingly chosen to be 1000 times longer. In Fig. 12(b), the E-field at the downstream point and the source waveform almost coincide since the time delay is

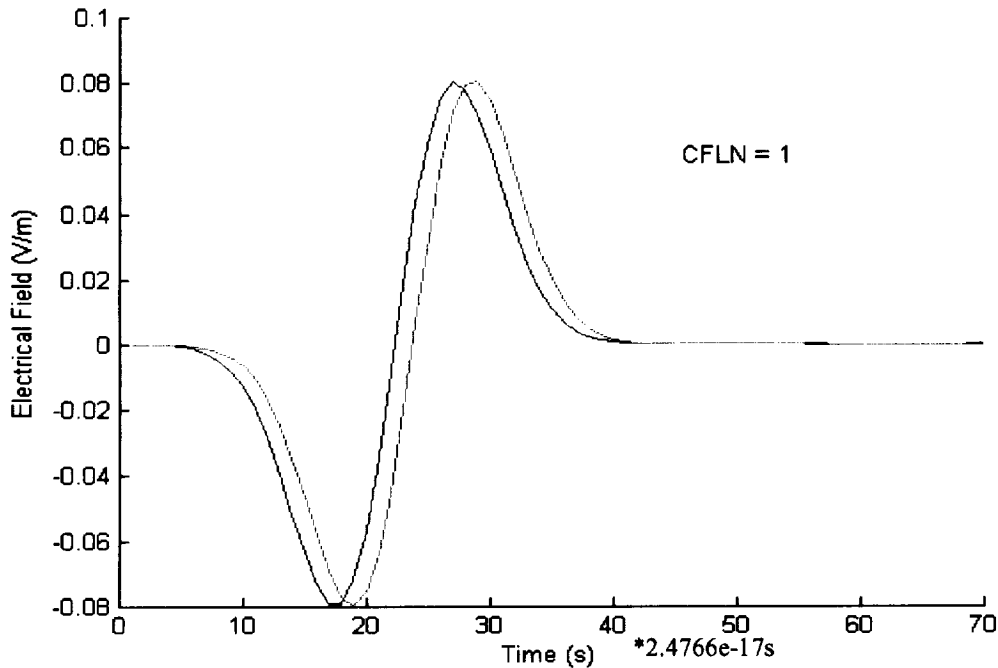


Fig. 12a. Source E-field pulse and E-field at an observation point downstream obtained from an ADI-FDTD solution. The time step was chosen to equal the CFL condition.

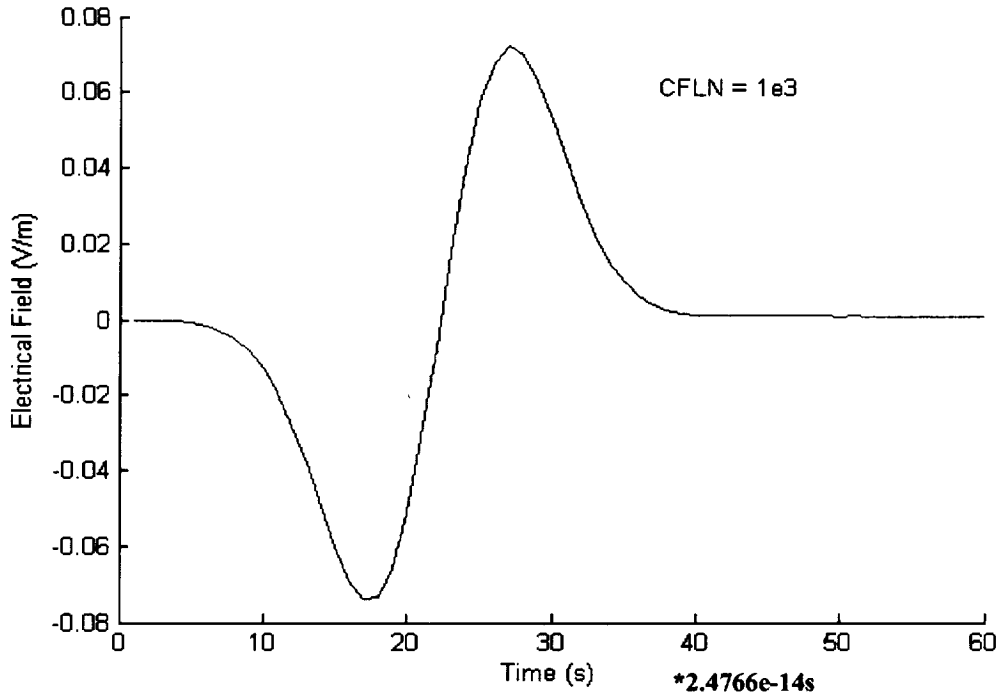


Fig. 12b. Source E-field pulse and E-field at an observation point downstream obtained from an ADI-FDTD solution. The time step was chosen to equal 1000 times the CFL condition.

very small compared on this new time-scale. The significant point, though, is that the field at the observation retains the same shape and does not cause any numerical instability despite the larger time step. Finally, a time step significantly larger ( $10^6$  times) the CFL requirement was used to check for the numerical stability of the ADI-FDTD code. The time-dependent electric fields of the source pulse (correspondingly taken to be  $10^6$  times larger), and at the observation point are shown in Fig. 12(c). Due to the large times, the delay between the E-fields of the source and at the observation point again cannot be discerned in the figure. However, both values were calculated and match the expected trend without any instability. This, conclusively demonstrates the successful implementation of an ADI-FDTD technique that can use time steps up to  $10^6$  times the CFL condition of traditional FDTD.

A second example is now presented and discussed with the aim of demonstrating a successful comparison between ADI-FDTD and traditional FDTD. However, in this case absorbing boundary conditions are implemented through a perfectly matched layer proposed by Berenger [30]. A source from an incident plane is used and a thin dielectric wall placed between the source plane and the

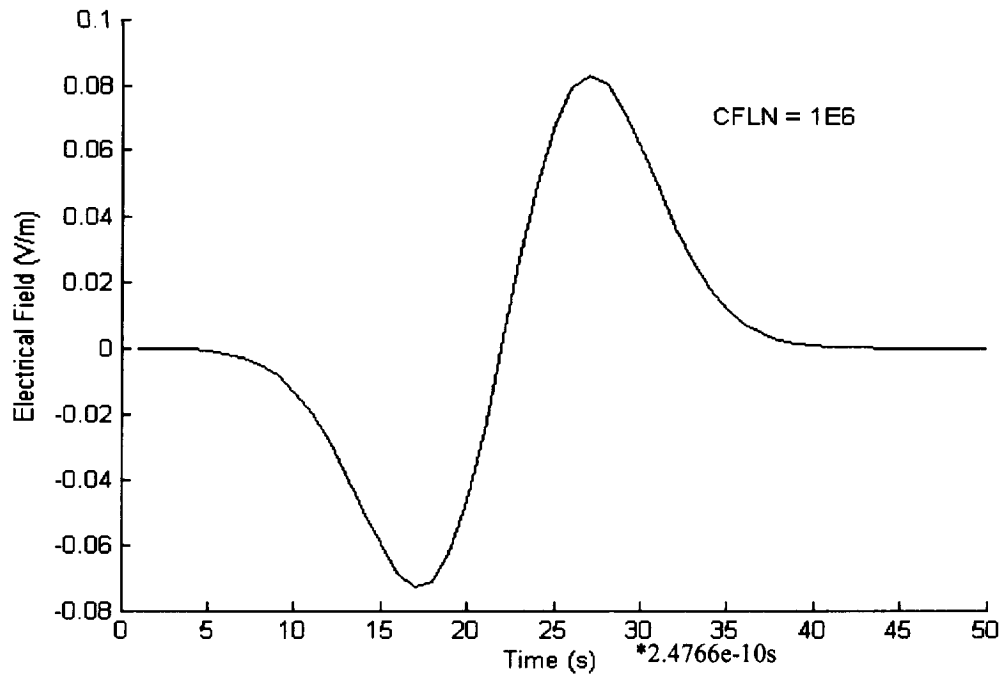


Fig. 12c. Source E-field pulse and E-field at an observation point downstream obtained from an ADI-FDTD solution. The time step was chosen to equal  $10^6$  times the CFL condition.

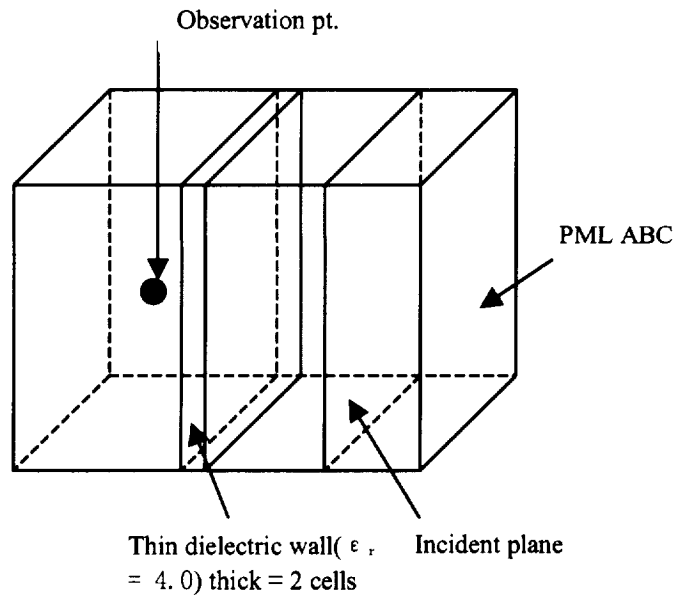


Fig. 13a. Geometry of a planar E-field source and an observation point separated by a thin dielectric.

observation point as shown in Fig. 13(a). For an incident sine wave, the electric field at the observation point as obtained by the ADI-FDTD method *in the absence of a dielectric wall* is shown in Fig. 13(b). Due to the finite separation, there is a time lag between the two curves. Fig. 13(c) shows the E-field output at the observation point with ADI-FDTD and the traditional FDTD techniques. The time step for the ADI technique was 8 times larger. Though larger time steps could have been chosen from a stability standpoint, it would then not have been possible to plot the values over the  $3.5 \times 10^{-10}$  s range of the graph. The close match between ADI-FDTD and the conventional FDTD is brought out clearly in Fig. 13(c).

The use of multi-grid meshes for solving ADI-FDTD problems is brought out through a final example. Shown in Fig. 14 is the geometry under consideration. It consists of an incident source plane, a surrounding PML region for absorbing boundary conditions, four observation points, and an embedded cube of water with a finite conductivity (to facilitate absorption) and a dielectric constant. The water cube was assumed to have a dielectric constant of 1.69, with a conductivity of 0.03 s/m. This cube was taken to have a material coating of conductivity 4.0 s/m and dielectric constant of 4.0.

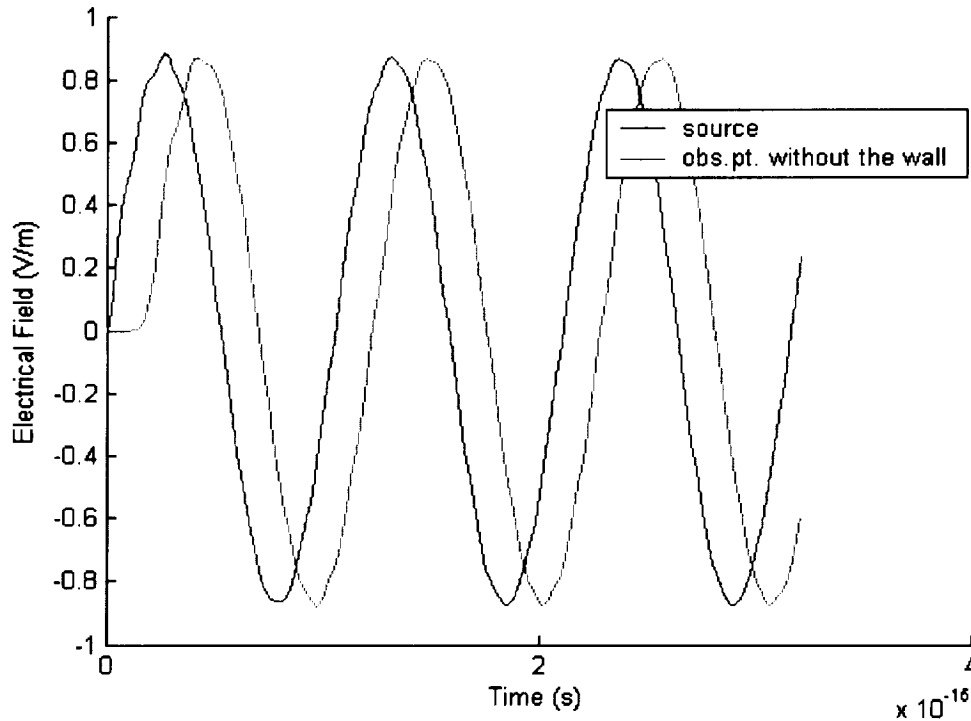


Fig. 13(b) Incident sine wave and the wave at the observation point without the dielectric wall.

Wavelength  $\lambda = 0.6328\mu\text{m}$ . Cell size =  $10.5*10.5*10.5$  nm.

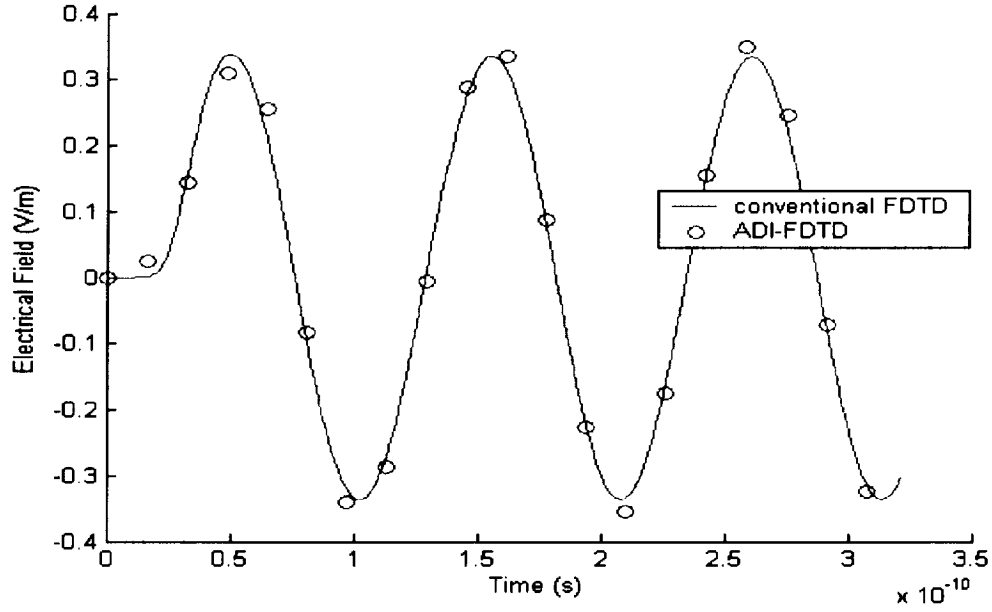


Fig. 13(c). Output wave at observation point calculated by conventional FDTD and ADI –FDTD. Time step for the conventional FDTD was  $2.022 \times 10^{-12}$ s and that for ADI-FDTD was  $1.618 \times 10^{-11}$ s.

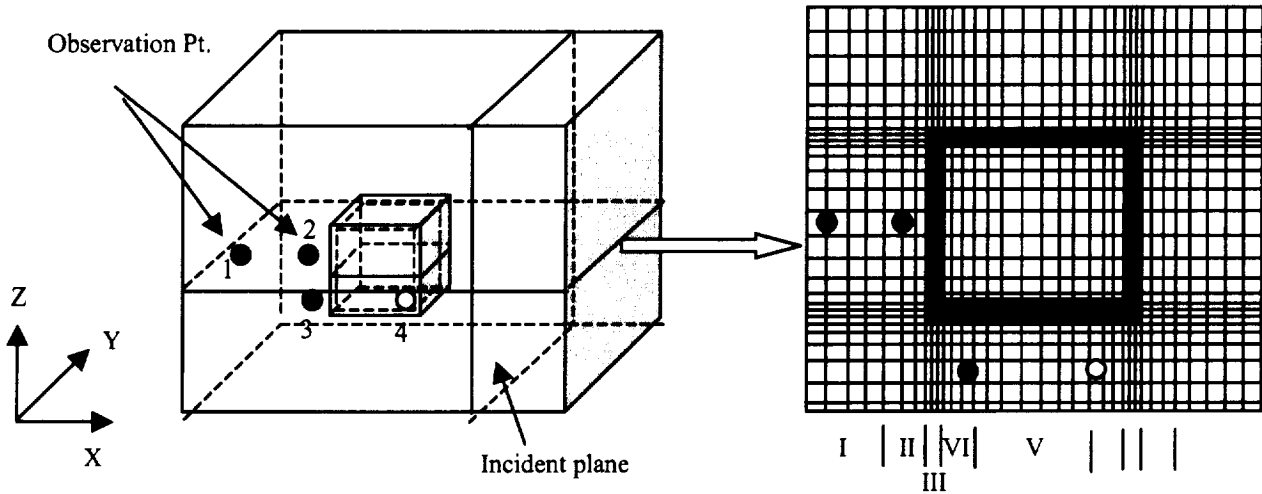


Fig 14. (a) A water cube ( $\sigma = 0.03\text{s/m}$ ,  $\epsilon_r = 1.69$ ) coated with material ( $\sigma = 4.0\text{s/m}$ ,  $\epsilon_r = 4.0$ )  
(b) Multi-sized grid in FDTD calculation.

The grid size was assigned as follows:  $\Delta x(i) = 1.05 \times 10^{-7} \text{ m}$  (in region I) ;  $\Delta x(i-1) \times 0.5$  (In region II);  $1 \times 10^{-8} \text{ m}$  (in region III) ;  $\Delta x(i-1) \times 2.0$  (in region IV) ; and  $= 1.05 \times 10^{-7} \text{ m}$  (in region V). The spacings  $\Delta y(i)$  and  $\Delta z(i)$  are defined in the same ways as  $\Delta x(i)$ . Fig. 15(a) shows the output waveform at observation point 2, and compares the results of FDTD and ADI-FDTD. The time steps were 0.02022 fs and 2.022 fs, respectively. CPU times of 2985 s and 257 s were required for the FDTD and ADI-FDTD schemes, respectively. The savings with the ADI technique are clear. The output at observation points 1 and 2 are given in Fig. 15(b).

#### X. Summary and Potential Future Work :

A study into the problem of determining electromagnetic solutions at high frequencies for problems involving complex geometries, large sizes and multiple sources (e.g. antennas) has been initiated. Typical applications include the behavior of antennas (and radiators) installed on complex conducting structures (e.g. ships, aircrafts, etc..) with strong interactions between antennas, the radiation patterns, and electromagnetic signals is of great interest for electromagnetic compatibility

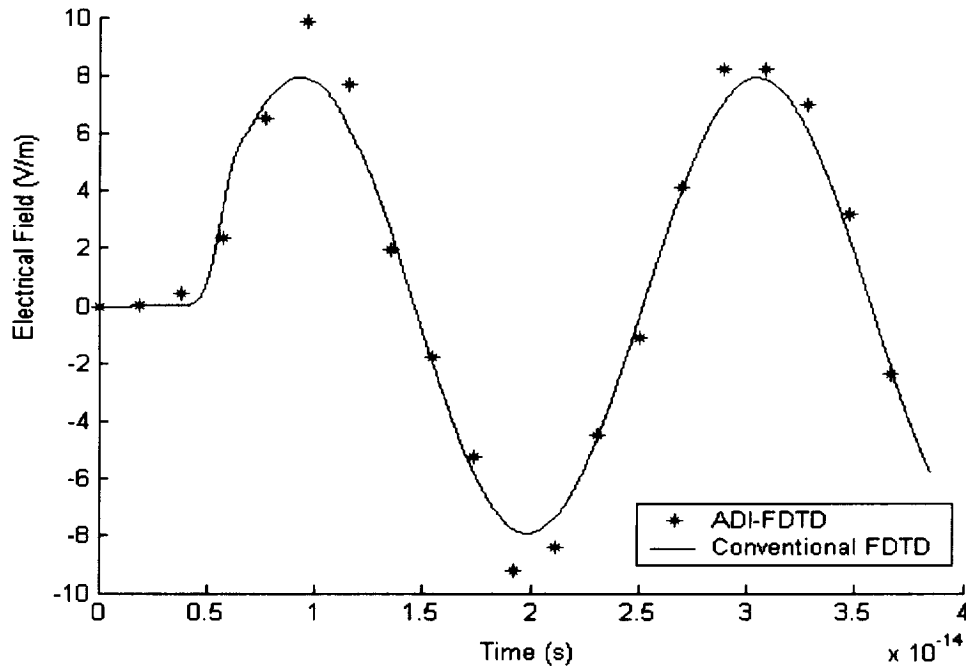


Fig. 15(a). Output waveform at the close observation point. CPU times: 257 s for ADI-FDTD, and 2985 s for conventional FDTD.



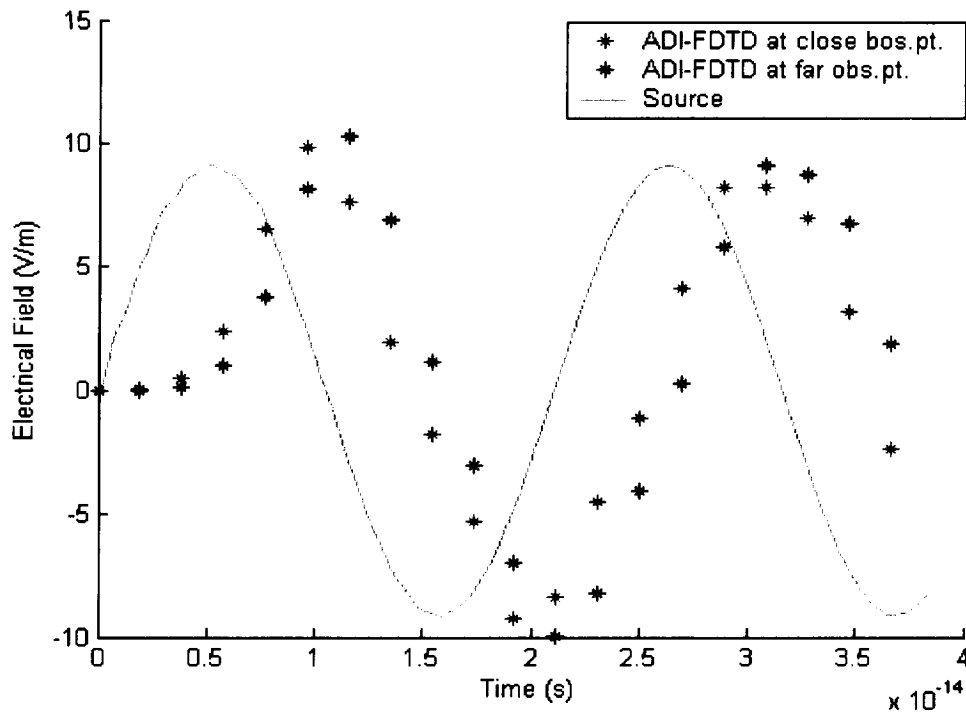


Fig. 15(b). Output at close observation point and far observation points 1 and 2.

control. This includes the overall performance evaluation and control of all on-board radiating systems, electromagnetic interference, and personnel radiation hazards.

Electromagnetic computational capability exists at NASA LaRC, and many of the codes developed are based on the Moment Method (MM). However, the MM is computationally intensive, and this places a limit on the size of objects and structures that can be modeled. Here, two approaches are proposed: (i) a current-based hybrid scheme that combines the MM with Physical optics, and (ii) an Alternating Direction Implicit-Finite Difference Time Domain (ADI-FDTD) method. The essence of a hybrid technique is to split the overall scattering surface(s) into two regions: (i) a MM zone (MMZ) which can be used over any part of the given geometry, but is most essential over irregular and “non-smooth” geometries, and (ii) a PO sub-region (POSR). Currents induced on the scattering and reflecting surfaces can then be computed in two ways depending on whether the region belonged to the MMZ or was part of the POSR. For the MMZ, the current calculations proceed in terms of basis functions with undetermined coefficients (as in the usual MM method), and the answer obtained by solving a system of linear equations. Over the POSR, conduction is obtained as a superposition of

two contributions: (i) currents due to the incident magnetic field, and (ii) currents produced by the mutual induction from conduction within the MMZ. This could effectively lead to a reduction in the size of linear equations from  $N$  to  $N - N_{PO}$  with  $N$  being the total number of segments for the entire surface and  $N_{PO}$  the number of segments over the POSR. The scheme would be appropriate for relatively large, flat surfaces, and at high frequencies.

The ADI-FDTD scheme is relatively new in the literature and was first proposed capable in 2000. It is capable of providing both transient and steady-state analyses. The primary advantage of this scheme is that large time-steps can be chosen without instability or inaccuracy, even though the spatial resolution is very small. Thus, computational speed enhancements of an order or more become possible. Hence, the ADI-FDTD method can be applied to problems involving large geometry, low wavelengths (i.e. high frequencies), and complex material characteristics such as composites and dielectric coatings.

This report includes the problem definition, a detailed discussion of both the numerical techniques, and numerical implementations for simple surface geometries. Numerical solutions have been derived for a few simple situations. The advantage of the ADI-FDTD scheme has been demonstrated. Future work in this area might include:

- (i) Direct comparison of numerical results from the present MM-code at NASA LaRC with ADI-FDTD results for simple geometries.
- (ii) Calculations for complex geometries and/or composite material properties including dielectric coatings.
- (iii) Expansion of the ODU codes to include wires, wire-surface and wire-wire interfaces.
- (iv) Use of the codes in the choice of materials and design for electromagnetic applications.

## **XI. References**

- [1] R. F. Harrington, *Field Computation by Moment Methods*. New York: MacMillian, 1968.
- [2]. R. Mittra, ed. *Computer Techniques for Electromagnetics*. New York: Pergamon Press, 1973.
- [3]. J. L. Volakis, A. Chatterjee, and L. C. Kempel, *Finite-Element Method for Electromagnetics: Antennas, Microwave Circuits, and Scattering Applications*. New York: IEEE Press, 1998.
- [4]. U. Jakobus and F. M. Landstorfer, IEEE Trans. Antennas Propagat., Vol. AP-43, pp. 162-169, 1995.

- [5]. P. H. Pathak, Proc. IEEE, Vol. 80, pp. 44-65, 1992.
- [6]. A. Sommerfeld and J. Runge, Ann. Phys. Vol. 35, pp. 277-298, 1911.
- [7]. M. Kline, Comm. Pure Appl. Math., Vol. 4, pp. 225-262, 1951.
- [8]. G. A. Thiele and T. H. Newhouse, IEEE Trans. Antennas Propagat., Vol. AP-23, pp. 62-69, 1975.
- [9]. W. D. Burnside, C. Yu, and R. J. Marhefka, IEEE Trans. Antennas Propagat., Vol. AP-23, pp. 551-558, 1975.
- [10]. G. A. Thiele, Proc. IEEE, Vol. 80, pp. 67-78, 1992.
- [11]. D. P. Bouche, F. A. Molinet, and R. Mittra, Proc. IEEE, Vol. 81, pp. 1658-1684, 1993.
- [12]. J. N. Sahalos and G. A. Thiele, IEEE Trans. Antennas Propagat., Vol. AP-29, pp. 780-786, 1981.
- [13]. W. D. Burnside, C. L. Yu, and R. J. Marhefka, IEEE Trans. Antennas Propagat., Vol. AP-23, pp. 551-558, 1975.
- [14]. L. N. Medgyesi-Mitschang and D. S. Wang, IEEE Trans. Antennas Propagat., Vol. AP-31, pp. 570-583, 1983.
- [15]. U. Jakobus and F. M. Landstorfer, IEEE Trans. Antennas Propagat., Vol. AP-43, pp. 1123-1129, 1995.
- [16]. R. E. Hodges and Y. Rahmat-Samii, IEEE Trans. Antennas Propagat., Vol. AP-45, pp. 265-276, 1997.
- [17]. F. Obelleiro, J. Rodriguez, and R. J. Burkholder, IEEE Trans. Antennas Propagat., Vol. AP-43, pp. 356-361, 1995.
- [18]. J. C. Veihl and R. Mittra, Scientific Report No. 93-2, Electromagnetic Communication Laboratory, University of Illinois Press, June 1993.
- [19]. S. M. Rao, D. R. Wilton, and G. W. Glisson, IEEE Trans. Antennas Propagat., Vol. AP-30, pp. 409-418, 1982.
- [20]. A. H. Stroud, *Approximate Calculation of Multiple Integrals*. Englewood Cliffs NJ: Prentice-Hall, 1971.
- [21]. D. R. Wilson, S. M. Rao, A. W. Glisson, D. H. Schaubert, O. M. Al-Bundak, and C. M. Butler, IEEE Trans. Antennas Propagat., Vol. AP-32, pp. 569-576, 1984.
- [22]. R. D. Graglia, IEEE Trans. Antennas Propagat., Vol. AP-41, pp. 1448-1455, 1993.
- [23]. L. N. Medgyesi-Mitschang and D. S. Wang, Annals of Telecommunications, Vol. 44, pp.

445-455, 1989.

- [24]. S. Srikanth, P. H. Pathak, and C. W. Chuang, *IEEE Trans. Antennas Propagat.*, Vol. AP-34, pp. 1250-1257, 1986.
- [25]. T. J. Kim and G. A. Thiele, *IEEE Trans. Antennas Propagat.*, Vol. AP-30, pp. 888-897, 1982.
- [26]. D. S. Wang, *IEEE Trans. Antennas Propagat.*, Vol. AP-39, pp. 839-850, 1991.
- [27]. J. M. Taboada, F. Obelleiro, and J. L. Rodriguez, *Microwave and Optical Technol. Lett.*, Vol.30, pp.357-63, 2001 ; F. Obelleiro, J. M. Taboada, J. L. Rodriguez, J. O. Rubinos, and A. M. Arias, *Microwave and Optical Technol. Lett.*, Vol.27, pp.88-93, 2000.
- [28]. K. Yee, "Numerical solutions of initial boundary value problems involving Maxwell's equations in isotropic media," *IEEE Trans. Antennas Propagat.*, Vol. AP-14, pp. 302-307, May 1966.
- [29]. A. Taflove, *Computational electrodynamics: The finite-difference, time-domain method* Boston: Artech House, 1995.
- [30]. J. P. Berenger, "A perfectly matched layer for the absorption of electromagnetic waves," *J. Computat. Phys.*, Vol. 114, pp.185-200, Oct. 1994.
- [31]. J. G. Blaschak and G. A. Kriegsmann, "A comparative study of absorbing boundary conditions," *J. Computat. Phys.*, Vol. 77, pp. 109-139, July 1988.
- [32]. G. Mur, "Absorbing boundary conditions for the finite-difference approximation of the time-domain electromagnetic-field equations," *IEEE Trans. Electromagn. Compat.*, Vol. EMC-23, pp. 377-382, Nov. 1981.
- [33]. Z. P. Liao, H. L. Wong, B. P. Yang, and Y. F. Yuan, "A transmitting boundary for transient wave analysis," *Sci. Sin. A*, Vol. 27, pp. 1063-1076, July 1984.
- [34]. A. Taflove and K. Umashankar, "Radar cross section of general three-dimensional structures," *IEEE Trans. Electromagn. Compat.*, Vol.25, pp.423-440, Nov. 1983.
- [35]. R. J. Luebbers, K. S. Kunz, M. Schneider, F. Hunsberger, "A finite-difference time-domain near zone to far zone transformation," *IEEE Transactions on Antennas & Propagation*, Vol. 39, pp.429-433, April 1991.
- [36]. S. M. Rao, *Time domain electromagnetics* San Diego: Academic Press, 1999.
- [37]. G. Mie, "Beitrage zur optik truber Medien, speziell kolloidaler Metallosungen," *Ann. Phys.*, Vol. 30, pp. 377-452, March 1908.
- [38]. J. Maier, S. Walker, S. Fantini, M. Franceschini, and E. Gratton, "Possible correlation

- between blood glucose concentration and the reduced scattering coefficient of tissues in the near infrared,” *Opt. Lett.*, Vol. 19, pp. 2062-2064, Dec. 1994.
- [39]. A. Brunsting and P. Mullaney, “Differential light scattering from spherical mammalian cells,” *Biophys. J.*, Vol.14, pp. 439-453, June 1974.
  - [40]. T. Namiki, “A new FDTD algorithm based on alternating direction implicit method,” *IEEE Trans. Microwave Theory Tech.*, Vol. 47, pp. 2003-2007, Oct. 1999.
  - [41]. G. D. Smith, *Solution of Partial Differential Equations*, Oxford Univ. Press, Oxford, U.K., 1965.
  - [42]. T. Namiki, “A 3D ADI-FDTD method – unconditionally stable time-domain algorithm for solving full vector Maxwell’s equations,” *IEEE Trans. Microwave Theory Tech.*, Vol. 48, pp. 1743-1748, Oct. 2000.
  - [43]. G. Liu and S. D. Gedney, , “Perfectly matched layer media for an unconditionally stable three-dimensional ADI-FDTD method,” *IEEE Microwave and Guided Wave Letters*, Vol. 10, pp. 261-263, July 2000.
  - [44]. G. Gouesbet, B. Maheu, and G. Grehan, “Light scattering from a sphere arbitrarily located in a Gaussian beam, using a Bromwich formulation,” *J. Opt. Soc. Am.*, Vol. 5, pp. 1427-1443, Sept. 1988.
  - [45]. F. Onofri, G. Grehan, and G. Gouesbet, “Electromagnetic scattering from a multilayered sphere located in a arbitrary beam,” *Appl. Optics*, Vol. 34, pp. 7113-7124, Oct. 1995.
  - [46]. B. R. Johnson, “Exact theory of electromagnetic scattering by a heterogeneous multiplayer sphere in the infinite-layer limit: effective-media approach,” *J. Optical Soc. Am.*, Vol. 16, pp. 845-852, April 1999.
  - [47]. J. Mourant, J. Freyer, A. Hielscher, A. Eick, D. Shen, and T. Johnson, “Mechanisms of light scattering from biological cells relevant to noninvasive optical-tissue diagnostics,” *Appl. Optics*, Vol. 37, pp. 3586-3593, June 1998.
  - [48]. Y. Shao, A. V. Maximov, I. G. Ourdev, W. Rozmus, C. E. Capjack, “Spectral method simulations of light scattering by biological cells,” *IEEE J.Quan. Electr.*, Vol. 37, pp. 617-625, May 2001.
  - [49]. A. N. Shvalov, J. T. Soini, A. V. Chernyshev, P. A. Tarasov, E. Soini, and V. P. Maltsev, “Light-scattering properties of individual erythrocytes,” *Appl. Opt.*, Vol. 38, pp. 230-235, Jan. 1999.